1. Introduction

Solid Oxide Fuel Cell (SOFC) has been developed as an electrical energy source because of its high efficiency, high energy density and low emission. SOFC operates at 800 – 1000 ^{o}C. At this range of temperature, a variety of the fuel can be fed into the SOFC such as natural gas and biogas. Unlike other types of fuel cell, there is no necessity for SOFC to apply noble catalyst to the electrode. In addition, at this high operating temperature, SOFC can be combined with gas turbines, increasing the system efficiency of the combined cycle.

Electrochemical reactions are taken place at the three phase boundary of both anode and cathode side. At the anode, oxidation reaction of fuel is occurred and, at the cathode, the reduction reaction of oxidant is occurred in which the enthalpy of the overall reaction is equal to the electrical energy added with heat from the polarisation effects (phenomena leads to a reduction of cell voltage from equilibrium when circuit is closed). Heat transfer and temperature distribution may differ in each material. This can induce the thermal mismatch among materials, resulting in stress and finally crack inside the cell. Therefore, it is necessary to develop a simulation to predict the temperature behaviour inside the cell in order to understand the phenomena taken place inside the cell.

To simulate the phenomena inside the cell, mass sink and source terms are applied to the model in terms of H_2 and O_2 consumed and H_2O produced. These are applied at the three phase boundary located in-between the electrolyte and electrodes of both anode and cathode sides. Conservation of momentum involves the momentum flow of reactants and products through the porous electrodes. These porous electrodes allow passage of reactants and products to travel to/from the interphase between electrodes and electrolyte. In conservation of energy equation, apart from the energy balance, there is a source term of energy equipped. This source term is simulated according to the polarisation effects occurred inside the PEN structure. Equations of conservation of gas species are also applied to the model to solve the problem with gas concentration and mass fraction.

Computation Fluid Dynamics (CFD) is used as a tool to predict behaviours occurred inside the cell. Mostly it is considered under steady-state condition. However, in this work a transient model of the SOFC is also considered. During start-up period, important phenomena have been taken place and relation among important parameter such as temperature and concentration will be observed. A good prediction of mechanism occurred inside the cell leads to a better understanding in phenomena taken place inside the cell. This can be further applied to the experiments to achieve the better performance of the SOFC.

Objectives

1. To study the mechanism of steam reforming, water-gas shift and electrochemical reactions inside the anode flow channel of the SOFC.
2. To study the temperature distribution and heat transfer inside the anode flow channel.

2. Mathematical model of internal reforming reaction in an anode flow channel of a planar solid oxide fuel cell

2.1. Introduction

Solid Oxide Fuel Cell operates at relatively high temperature with hydrogen as a fuel fed to the anode flow channel and air as an oxidant fed to the cathode flow channel. To produce hydrogen, internal reforming of methane within an SOFC to produce hydrogen can maximize the efficiency and simplicity of the process by combining the reforming and electrochemical processes. Steam reforming is a highly endothermic reaction, whereas electrochemical oxidation is an exothermic reaction [1-4].

In order to obtain a better understanding of the SOFC operation, a number of theoretical models have been developed. Some studies have modelled various SOFC geometries [5-9]. Nevertheless, there are few investigations taking the influences of distributions of outcome components into consideration. In the present study, such work will be conducted by the model developed for planar anode-supported SOFC with internal methane steam reforming reaction based on a variety of steam to carbon ratio.

2.2. Model description

The two-dimensional model has been developed for the anode-supported planar SOFC. The conservation of mass, momentum and energy are taken into account including kinetics of electrochemical and chemical reactions. The details of the mathematical modelling are presented as follows:

2.2.1. Domain of consideration

The cell has been designed involving "ribbed" channels which act as both current collectors and flow directors as seen in Fig. 2.1. The anode flow channel which is 1 mm high and 50 mm long has been developed in this work with the anode thickness of 0.1 mm. The anode has the density of 6950 kg/m^3, conductivity of 3 W/mK and specific heat of 400 J/kgK. In this two-dimensional mathematical model, the steady-state condition and laminar incompressible flow are assumed. Radiative heat transfer is negligible.

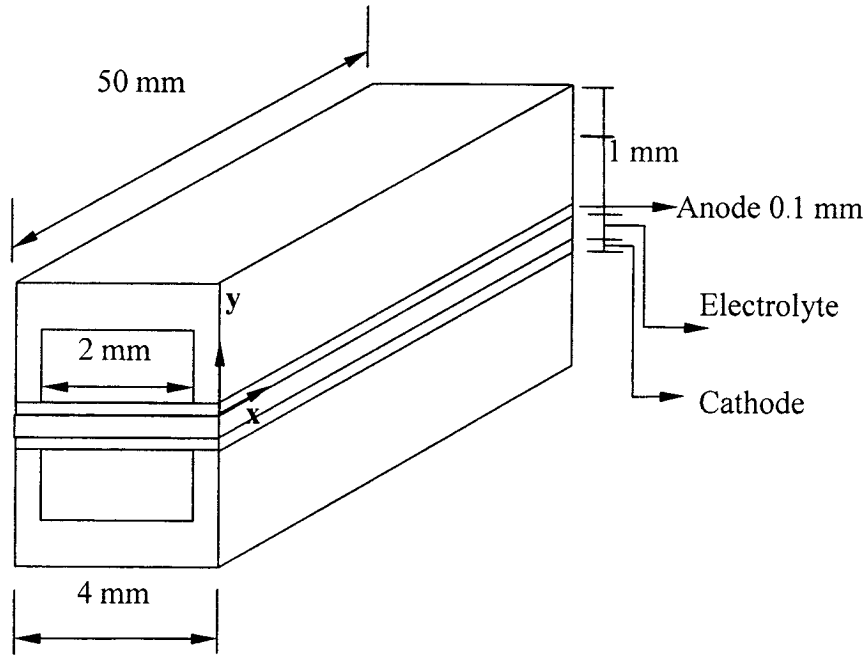

Figure 2.1. Schematic diagram of a fuel cell model.

2.2.2. Governing equations

In this model, the governing equations of mass, momentum, and energy as shown in Eqs. (2.1)-(2.3) are applied to the computational domain to calculate the concentration, velocity and temperature profiles within the domain.

Conservation of mass:

$$\nabla \cdot (\rho u) = 0 \tag{2.1}$$

Conservation of momentum:

$$-\nabla \cdot \mu(\nabla u) + \rho u \cdot \nabla u + \nabla p = 0 \tag{2.2}$$

Conservation of energy:

$$\nabla \cdot \left(-k\nabla T + \rho C_p T u\right) = Q \tag{2.3}$$

In addition, convection and diffusion of various gas species in the flow channel must be involved in the computational domain, thus the conservation of mass species can be expressed in Eq.(2.4) as

$$\nabla \cdot \left(-D_i \nabla c_i + c_i u\right) = R_i \tag{2.4}$$

2.2.3. Chemical and electrochemical reactions

Due to the fact that methane (CH_4), which is fed to the anode compartment, can be reformed and shifted into hydrogen (H_2) through steam reforming and water-gas shift reactions as shown in Eqs. (2.5) and (2.7), the rate of steam reforming and water-gas shift

reactions are also considered in the anode domain as shown in Eqs. (2.6) and (2.8), respectively.

Steam reforming reaction:

$$CH_4 + H_2O \rightarrow 3H_2 + CO \quad (2.5)$$

Rate of steam reforming reaction [10]:

$$R_r = k_o p_{CH_4} e^{(-E_a/(RT))} \times A_v \quad (2.6)$$

Water-gas shift reaction:

$$CO + H_2O \rightarrow CO_2 + H_2 \quad (2.7)$$

Rate of water-gas shift reaction [10]:

$$R_s = k_{wgs} p_{H_2O} p_{CO} \left(1 - \frac{p_{H_2} p_{CO_2}}{p_{H_2O} p_{CO} K_{s,eq}}\right) \quad (2.8)$$

Finally, the rate of production of each gas species can be formulated as shown in Eqs. (2.9) to (2.13) [3,11]:

$$R_{CH_4} = -R_r \quad (2.9)$$

$$R_{CO} = -R_r - R_s \quad (2.10)$$

$$R_{H_2O} = -R_r - R_s \quad (2.11)$$

$$R_{H_2} = 3R_r + R_s \quad (2.12)$$

$$R_{CO_2} = R_s \quad (2.13)$$

Heat source term, Q (W/m^2), in Eq. (3) can be defined according to the heat of reaction of the steam reforming, water-gas shift and oxidation reactions as shown in Eqs. (2.14) [12] and (2.15) [13].

$$Q = (R_r \times \Delta H_r) + (R_s \times A_v \times \Delta H_s) + \left(\frac{-\Delta H_{ox}}{2F} \times i\right) - (i \times v_{cell}) \quad (2.14)$$

$$\Delta H_{ox} = -(240506 + 7.3835T) \quad (2.15)$$

Electrons flow from the anode to the cathode through the external circuits. Consequently the electric current is produced. The overall reaction expressed in Eq. (2.16) is assumed as a boundary condition in the vicinity of the electrolyte/anode interphase where the mass sink and source are determined in Eqs. (2.17) and (2.18) followed by Eqs. (2.19) and (2.20), defining i_o and $i_{o,an}$.

Overall reaction: $H_2 + \frac{1}{2}O_2 \rightarrow H_2O + Electricity + Heat$ (2.16)

H_2 consumption: $$S_{H_2} = -\frac{i}{2F} \quad (2.17)$$

H_2O consumption: $$S_{H_2O} = \frac{i}{2F} \quad (2.18)$$

$$i = i_{o,an}\left(\frac{p_{H_2}}{p_{H_2in}}\exp^{F\eta/RT} - \frac{p_{H_2O}}{p_{H_2O_{in}}}\exp^{(-F\eta/RT)}\right) \quad (2.19)$$

$$i_{o,an} = \frac{RT}{2F}k_{an}\exp^{-E_{an}/RT} \quad (2.20)$$

2.2.4. Boundary conditions

It is assumed that the steam reforming and water-gas shift reaction are occurred on the anode surface whereas the oxidation reaction is assumed at the anode/electrolyte interphase. At this interphase, mass source and sink due to the oxidation reaction as expressed in Eqs. (2.17) and (2.18) are applied. At the channel inlet, the fuel flow is defined at 2 m/s and 1123 K. Heat source due to steam reforming, water-gas shift and oxidation reactions as expressed in Eqs. (2.14) and (2.15) is applied at the anode/electrolyte interphase. At the channel outlet, the normal flow and convection are assumed.

2.3. Numerical implementation

The governing equations equipped with kinetic equations of the steam reforming, water-gas shift and electrochemical reactions are solved using the Finite Element Method technique. Structured mesh elements are composed of 2D rectangles with 1000 elements contained in the computational domain.

2.4. Results and discussions

It is realized that carbon can be generated during methane steam reforming in high temperature environment. Although most of the carbon is converted into CO, CO_2 and H_2, some of carbon still remains. The carbon deposition may lead to the catalyst toxicosis [10]. According to the reactions, carbon generated increases with decreasing H_2O mass fraction at the inlet surface. This indicates that the carbon deposition can be prevented by increasing the inlet steam mass fraction or a steam to carbon ratio. Therefore, in this work, the steam to carbon ratios of 2:1, 3:1, 4:1 and 5:1 are considered.

Figs 2.2 to 2.5 depict the mass concentration of gas species along the anode surface with the different inlet steam to carbon ratios of 2:1, 3:1, 4:1 and 5:1, respectively. The concentration of CH_4 at the inlet in each case is different as illustrated in Fig. 2.6; however, the same decreasing trend applies to all cases due to the high rate of reaction. It can be seen that, with the steam to carbon ratio of 2:1, the mass concentration of CH_4 at the inlet is the highest.

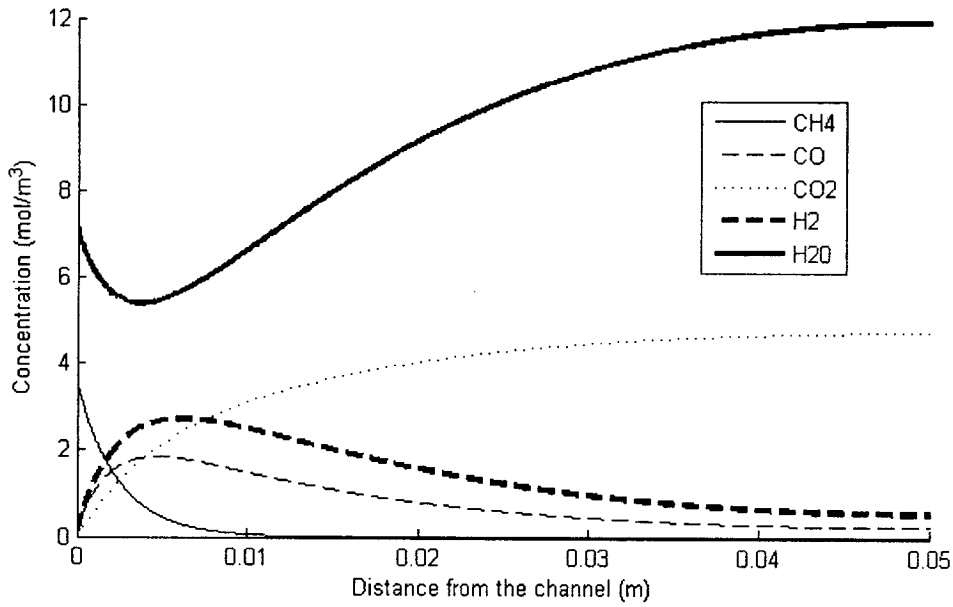

Figure 2.2. Mass concentration of gases along the anode surface with S/C = 2.

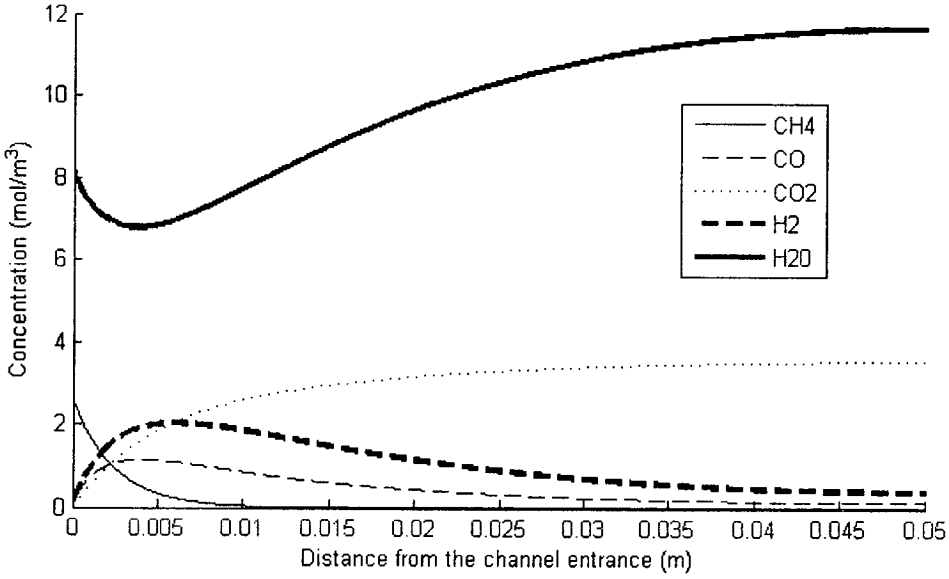

Figure 2.3. Mass concentration of gases along the anode surface with S/C = 3.

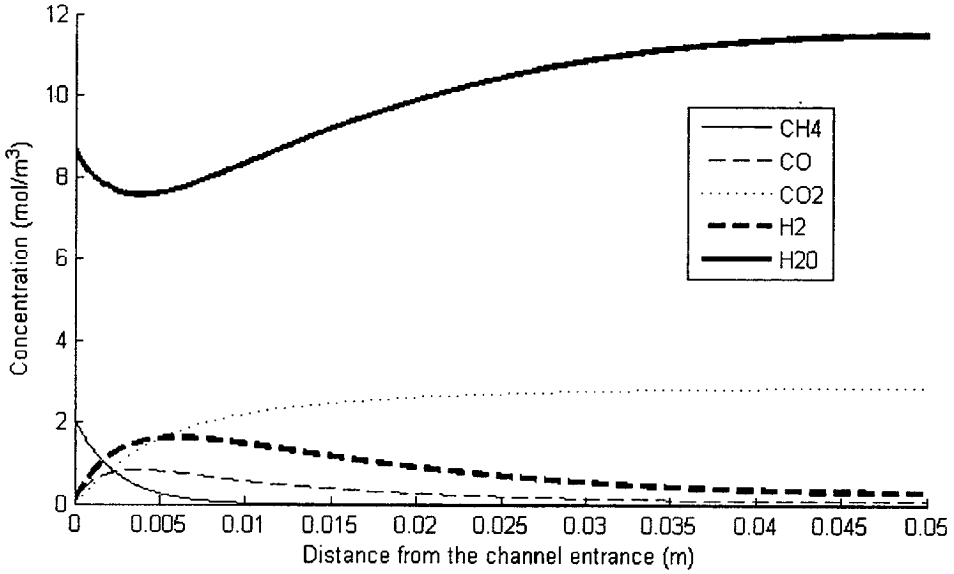

Figure 2.4. Mass concentration of gases along the anode surface with S/C = 4.

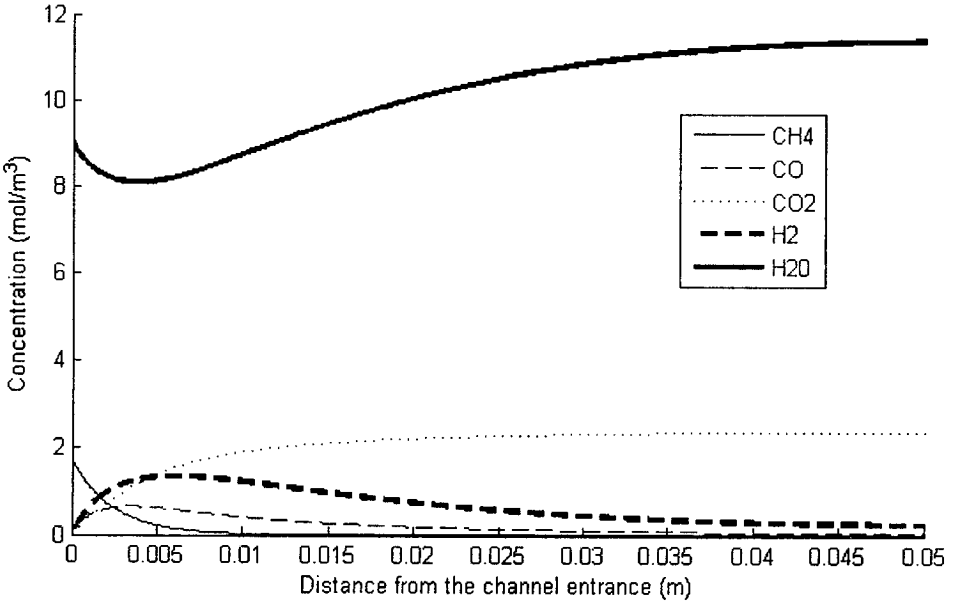

Figure 2.5. Mass concentration of gases along the anode surface with S/C = 5.

It can be seen in Fig. 2.6 that at all ratios, CH_4 is converted immediately near the flow channel inlet as the high reaction rate of the steam reforming reaction is occurred. H_2O is also consumed by steam reforming and water-gas shift reactions; as a result, the concentration is reduced near the inlet. However, H_2O is also produced through the electrochemical reaction, thus making the mass concentration of H_2O gradually increase throughout the flow channel as seen in Figs. 2.2 to 2.5. CO is produced by steam reforming reaction as consumed by water-gas shift reaction. The mass concentration of CO increases

significantly near the inlet according to the high rate of the steam reforming reaction, and gradually decreases as water-gas shift reaction has more effect on CO consumption.

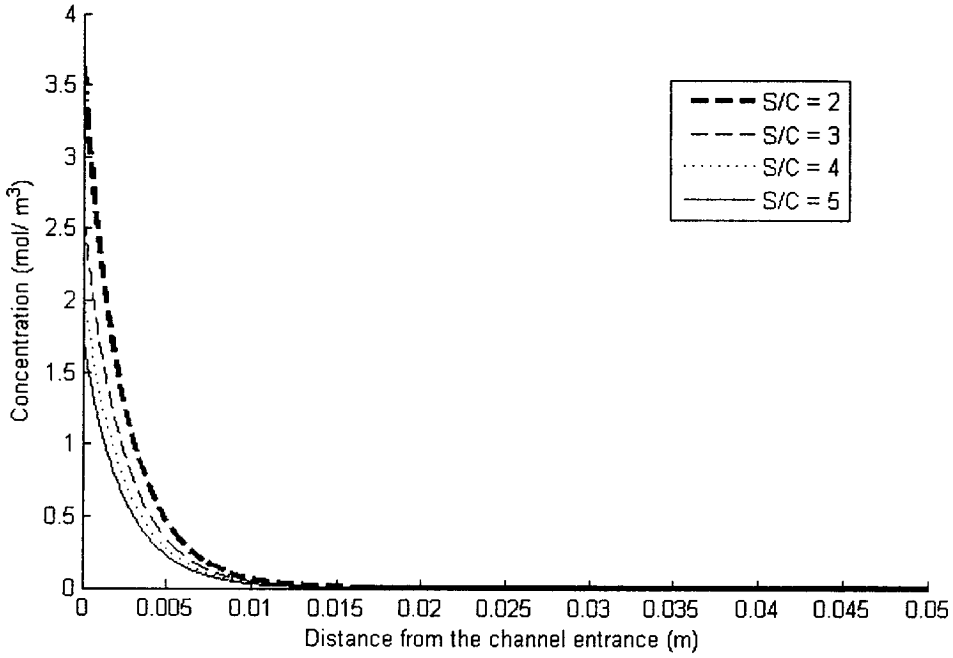

Figure 2.6. Mass concentration of CH_4 along the anode surface with different S/C.

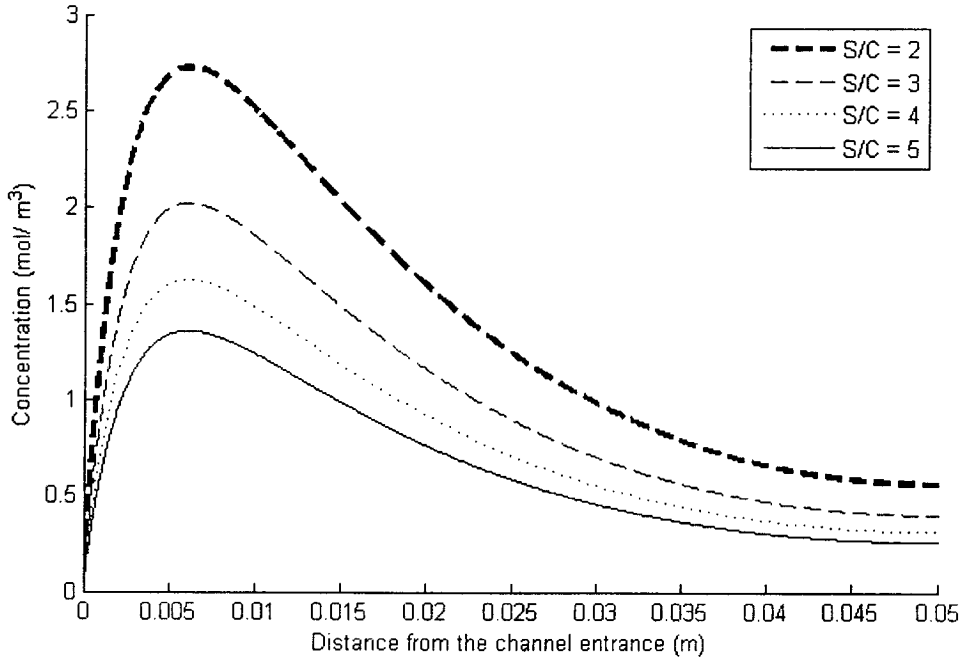

Figure 2.7. Mass concentration of H_2 along the anode surface with different S/C.

H_2 is produced by both steam reforming and water-gas shift reactions; nevertheless, as depicted in Figs. 2.2-2.5 and 2.7, it is consumed by electrochemical reaction, thus making the

H_2 mass concentration drop remarkably after reaching the maximum concentration near the inlet where the high rate of steam reforming reaction and water-gas shift reaction occur. An increase in the concentration applies to CO_2 mass concentration trend which is produced by the water-gas shift reaction. As a consequence, an increase of CO along the flow channel can be found in Figs. 2.2-2.5.

The plots in Figs. 2.2 to 2.5 agree well with the rate of steam reforming reaction plotted in Fig. 2.8 where the steam to carbon ratio of 2:1 represents the highest rate of reaction. From Figs. 2.6 and 2.8, it can be observed that the higher the steam to carbon ratio, the lower the amount of CH_4 and the rate of the reaction. Finally, Fig. 2.7 illustrates that at the steam to carbon ratio of 2:1, the amount of H_2 produced is the largest after compared with other steam to carbon ratios.

The anode flow channel is assumed to be insulated all sides. Heat sink and source terms are calculated from the heat of reaction from steam reforming, water-gas shift and oxidation reactions occurring on the electrolyte surface. Heat is conducted through the anode layer and then convected by the gas flow in the anode flow channel. Fig. 2.9 illustrates the temperature profile at the solid phase along the anode flow channel. According to Fig. 2.9, it can be found that the temperature is rapidly decreased near the inlet where the rate of the endothermic steam reforming reaction is at its highest. Subsequently, the temperature is gradually decreased as the effect of endothermic reaction still remains.

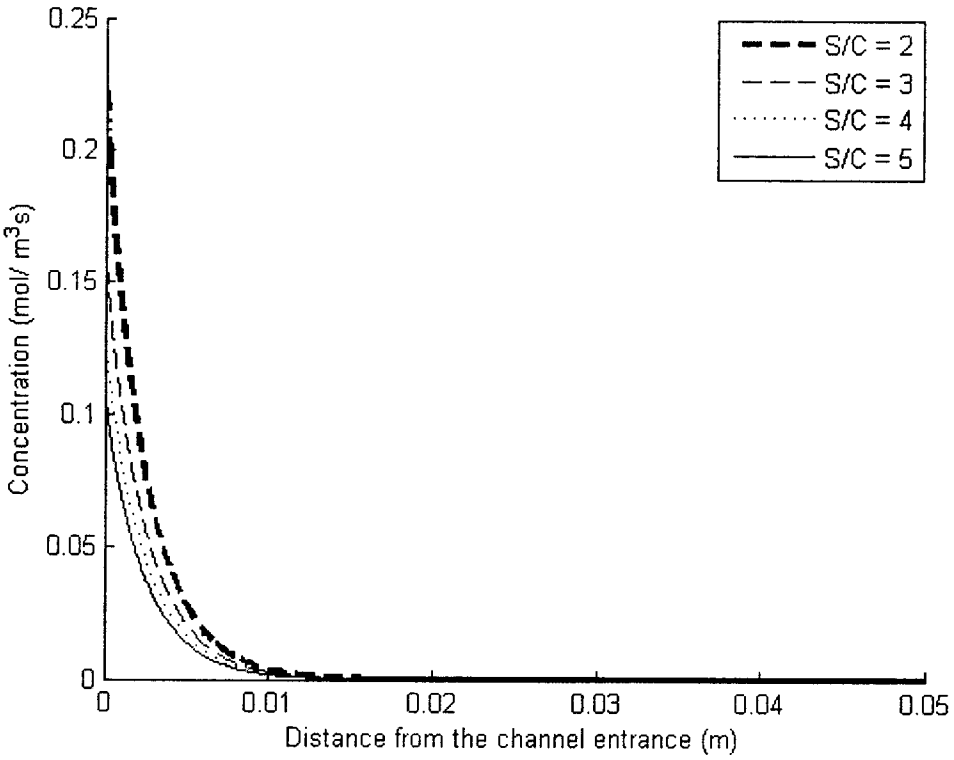

Figure 2.8. Rate of reforming reaction along the anode surface with different S/C.

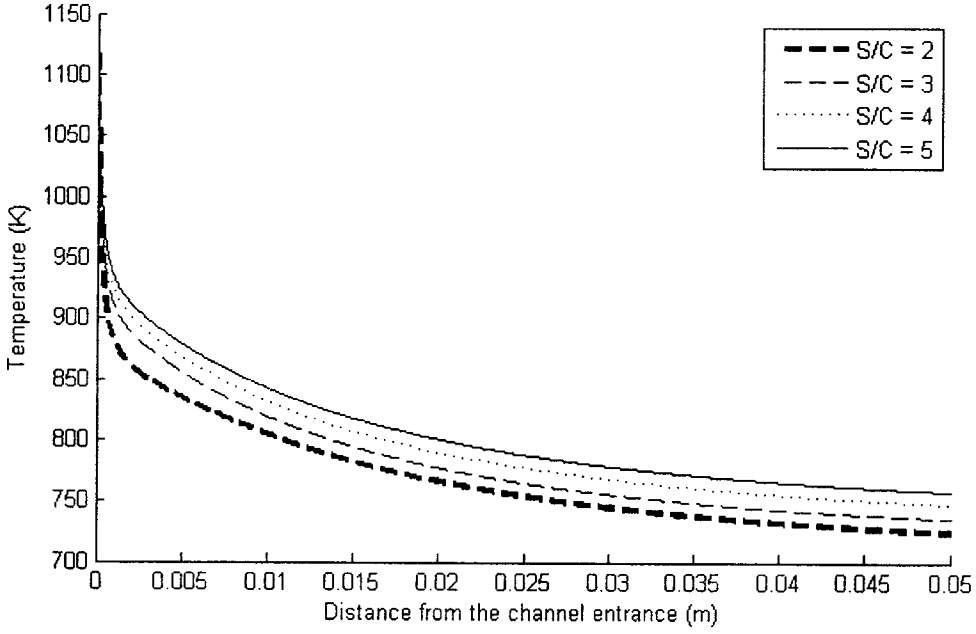

Figure 2.9. Temperature along the anode surface.

3. The effect of anode porosity on the transport phenomena in an anode-supported solid oxide fuel cell

3.1. Introduction

Solid oxide fuel cell (SOFC) is a type of fuel cells which has been developed over a long period of time as an electrical energy source due to its high efficiency, high energy density and low emission. SOFC operates at high temperature from 800 to 1000°C, a suitable condition for reforming reaction to occur in the anode flow compartment. Hydrocarbons, once reacting with steam under a suitable condition, produce hydrogen which is consequently used as a fuel in the anode compartment. Therefore, fuel used in SOFC is more flexible than that of other fuel cell types. In addition, catalysts made of noble materials are not required in the cell. Above all, SOFC can be combined with a gas turbine system to obtain a higher overall electrical efficiency.

The electrode-supported SOFC has a thick either porous anode or cathode and a thin electrolyte. Attention has been drawn to the anode-supported SOFC lately due to the lower ohmic loss in the electrolyte and a wider operating range of current density resulting in the higher power density after compared with the cathode-supported [14]. Over the recent years, a theoretical study of SOFC has been extensively carried out and considerable modelling work of anode-supported SOFC has been developed using a Computational Fluid Dynamics technique. Numerous models have been developed to calculate the transport of gases and current density by assuming H_2- H_2O mixture as a fuel [4, 9, 15-17]. The transport phenomena inside the cell, including gas flow behaviour, species concentration, overpotential and current density were simulated. Jeon [17] and Shi et al. [9] revealed that temperature, gas concentration, anode thickness and cathode surface area have influences on the fuel cell performance. Additionally, some work has considered the kinetics of the steam reforming reaction and the shift reaction, thus the cooling and heating effects of endothermic and exothermic reactions can be studied. This includes the work of Lehnert et al. [3] who developed a 1-D model to describe the transport of gases inside the SOFC with a consideration of the kinetics of the reforming reaction and the electrochemistry. Similarly, mathematical planar SOFC models which are fuel flexible have been developed in order to examine the effect of various operating and design parameters on the performance of SOFC within different geometries where characteristics of steam reforming reaction in porous anode support are considered to disclose the performance of SOFCs with the effects of binary and Knudsen diffusion accounted in the porous electrodes [6, 12, 18-21]. Hussain et al. [6] and Ni et al [20] also found that a thick porous anode could cause the higher ohmic and concentration overpotentials on the anode side than those on the cathode side.

Nonetheless, it has been found from literature review that an effect of porous structure has been slightly investigated. Hussain et al. [6] observed that an increase of the porosity of the cell components has decreased the cell performance; however, an increase of the tortuosity of the porous layers has decreased the performance of the cell. Ni et al. [20] found that both porosity grading and pore size grading were effective to increase the SOFC working potential due to the reduced concentration overpotential. Yang et al [21] indicated that the porous structure with the porosity of 0.4 may be the most appropriate configuration for internal reforming of integrated-planar SOFC (IP-SOFC). Therefore, in this study, a mathematical model with a consideration of the steam reforming reaction and the shift reaction has been developed to study the effect of the anode porosity on the gas species, temperature and current density distributions on the anode side of the anode-supported Solid Oxide Fuel Cell (SOFC). The models of mass, momentum and energy are developed where the variation of porosity affecting other relevant parameters such as permeability and tortuosity will be investigated.

3.2. Model development

The two-dimensional model has been developed for the anode-supported planar SOFC. The conservation of mass, momentum and energy are taken into account including the conservation of charge, and kinetics of electrochemical and chemical reactions. The details of the mathematical modelling are presented as follows:

3.2.1. Geometry, properties and assumptions

The cell has been designed involving "ribbed" channels which act as both current collectors and flow directors. The 1 mm high and 50 mm long anode and cathode flow channels have been developed in this work according to Fig. 3.1. Further details of dimensions and physical properties are given in table 3.1 [22].

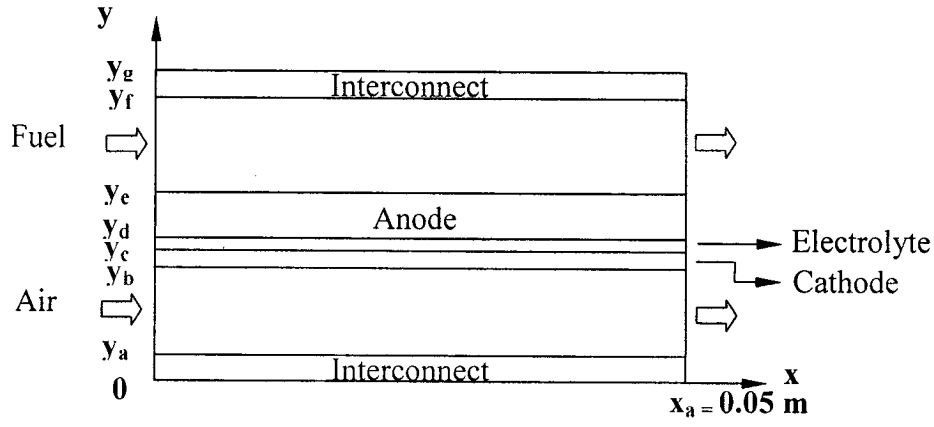

Figure 3.1. Schematic diagram of a fuel cell model

Table 3.1. Dimensions and physical properties of cell components.

Material	Thickness (μm)	Density (kg/m^3)	Conductivity (W/mK)	Specific heat (J/kgK)
Electrolyte	20	5900	2	550
Anode	500	6950	3	400
Cathode	50	6580	3	300
Interconnect	500	6600	3.5	400

This mathematical modelling has been developed based on assumptions as follows:

(1) The model is based on two-dimensional flow under steady-state condition.

(2) The reactant gas mixtures are ideal gases.

(3) Gas flow in the channel is laminar.

(4) Incompressible flow is assumed.

(5) Radiative heat transfer is negligible.

3.2.2. Transport equations

In this model, the governing equations of mass, momentum and energy including the charge conservation are applied to the computational domain to calculate the concentration, velocity, temperature and potential profiles within the domain. The governing equations are consequently solved by the Computational Fluid Dynamics (CFD) technique through Eqs. (3.1-3.3).

Conservation of mass:

$$\nabla \cdot (\rho u) = 0 \tag{3.1}$$

Conservation of momentum:

$$-\nabla \cdot \left[\mu \left(\nabla u + (\nabla u)^T \right) \right] + \rho u \cdot \nabla u + \nabla p = 0 \tag{3.2}$$

Conservation of energy:

$$\nabla \cdot \left(-k \nabla T + \rho C_p T u \right) = Q \tag{3.3}$$

Convection and diffusion of various gas species in the flow channel must be involved in the computational domain, thus the conservation of mass species can be expressed in Eq.(3.4) as

$$\nabla \cdot \left(-D_i \nabla c_i + c_i u \right) = R_i \tag{3.4}$$

Conservation of charge:

The ionic charge conservation equation is applied to the electrolyte layer according to Eq.(3.5).

$$-\nabla \cdot \left(\sigma_e \nabla \phi_e \right) = 0 \tag{3.5}$$

and σ_e can be defined in Eq. (3.6) as

$$\sigma_e = \frac{1}{3\times10^{-5}\exp(10300/T)}$$

(3.6)

The electronic charge conservation equation as expressed in Eq.(3.7) is applied to both cathode and anode

$$-\nabla\cdot(\sigma_s\nabla\phi_s) = 0$$

(3.7)

with the expression of σ_s as shown in Eq. (3.8)

anode: $$\sigma_s = \frac{1}{2.98\times10^{-5}\exp(-1392/T)}\times\frac{(1-\varepsilon)}{\tau} \quad (3.8)$$

It is difficult to determine the suitable model expressing the relation between the tortuosity (τ) and the porosity (ε) of the porous media. The correlation in Eq. (3.9) [23, 24] is then selected as it is found in a theoretical study on diffusivity of a model porous system.

$$\tau = 1-0.50\ln(\varepsilon) \quad (3.9)$$

When the calculation domains are both anode and cathode, the conservation of momentum is expressed by Eq. (3.10).

$$-\nabla\cdot\left[\mu\left(\nabla u+(\nabla u)^T\right)\right]+\nabla p = -\frac{\mu}{k_p}u \quad (3.10)$$

and k_p is defined in Eq. (3.11) [17] as

$$k_p = \frac{\varepsilon^3}{180(1-\varepsilon)^2}d_p^2 \quad (3.11)$$

D_i is the effective mass diffusivity of component i in the porous media, and can be expressed in Eq. (3.12) [4] as:

$$D_i = \frac{\varepsilon}{\tau}\left(\frac{1-\alpha_{im}y_i}{D_{i,m}}+\frac{1}{D_{Ki}}\right)^{-1} \quad (3.12)$$

with α_{im} defined in Eq. (3.13) as

$$\alpha_{im} = 1-\left(\frac{M_i}{M_m}\right)^{1/2} \quad (3.13)$$

The Knudsen diffusion coefficient for the component i in the multi-component mixture gas is expressed in Eq. (3.14):

$$D_{Ki} = \frac{2}{3}\left(\frac{8RT}{\pi M_i}\right)^{1/2}\bar{r} \quad (3.14)$$

For the gas mixture, the diffusivity is defined in Eq.(3.15) as;

$$D_{i,m} = \frac{1-y_i}{\sum_{k\neq i}^{n}\frac{y_k}{D_{ik}}} \quad (3.15)$$

The binary diffusivity, D_{ik}, can be calculated from the equation of Fuller et al. [25] in Eq. (3.16);

$$D_{ik} = \frac{0.00143T^{1.75}}{PM_{ik}^{1/2}\left[(\Sigma_v)_i^{1/3} + (\Sigma_v)_k^{1/3}\right]^2} \quad (3.16)$$

In addition, the effective thermal conductivity (k_{eff}) as shown in Eq. (3.17) [11, 21] will be used in Eq. (3) when energy conservation in electrodes is considered.

$$k_{eff} = (1-\varepsilon)k_s + \varepsilon k_g \quad (3.17)$$

3.2.3. Chemical reactions

Due to the fact that methane (CH_4) can be reformed and shifted into hydrogen (H_2) through steam reforming and water-gas shift reactions as shown in Eqs. (3.18) and (3.20), the rate of the steam reforming reaction and the water-gas shift reaction are also considered in the anode domain as shown in Eqs. (3.19) and (3.21), respectively.

Steam reforming reaction: $CH_4 + H_2O \rightarrow 3H_2 + CO$ (3.18)

Rate of steam reforming reaction [1]: $R_r = k_o p_{CH_4} e^{(-E_a/(RT))} \times A_v$ (3.19)

Where A_v is the reactive surface area per unit volume ($m^2 m^{-3}$) [6, 26]. The calculation of A_v is based on the assumption that the radii of the electron and ion conducting particles equal 0.1 μm.

Water-gas shift reaction: $CO + H_2O \rightarrow CO_2 + H_2$ (3.20)

Rate of water-gas shift reaction [2, 3, 11]:

$$R_s = k_{wgs} p_{H_2O} p_{CO}\left(1 - \frac{p_{H_2} p_{CO_2}}{p_{H_2O} p_{CO} K_{s,eq}}\right) \quad (3.21)$$

Finally, the rate of production of gas species can be formulated as shown in Eqs. (3.22) to (3.26) [3,18]:

$$R_{CH_4} = -R_r \quad (3.22)$$

$$R_{CO} = -R_r - R_s \quad (3.23)$$

$$R_{H_2O} = -R_r - R_s \quad (3.24)$$

$$R_{H_2} = 3R_r + R_s \quad (3.25)$$

$$R_{CO_2} = R_s \quad (3.26)$$

Heat source term, Q (W/m^3), in Eq. (3.3) can be defined according to the heat of reaction of the steam reforming reaction and the water-gas shift reaction as shown in Eqs. (3.27), (29)-(3.30). In addition, there is also a heat source term at the anode/electrolyte interface due to the emerging of oxidation reaction as expressed in Eqs. (3.28) and (3.31).

$$Q = (R_r \times \Delta H_r \times A_v) + (R_s \times \Delta H_s) \quad (3.27)$$

$$Q_{ox} = \left(\frac{-\Delta H_{ox}}{2F} \times i\right) - (i \times v_{cell}) \quad (3.28)$$

$$\Delta H_r = 60.8T - 0.0196T^2 - 1.202e^{-5}T^3 + 6.2828e^{-9}T^4 + 189985.4665 \quad (3.29)$$

$$\Delta H_s = -43729 + 9.4657T \quad (3.30)$$

$$\Delta H_{ox} = -(240506 + 7.3835T) \quad (3.31)$$

3.2.4. Electrochemical reactions

Anodic current density (i_a) and anodic exchange current density ($i_{o,an}$) can be defined as Eqs. (3.32) [27] and (3.33) [28] as well as cathodic current density (i_c) and cathodic exchange current density ($i_{o,cat}$) in Eqs. (3.34) [27] and (3.35) [28].

$$i_a = i_{o,an}\left(e^{(1-\beta)\eta F/RT} - e^{-\beta\eta F/RT}\right) \quad (3.32)$$

$$i_{o,an} = \gamma_a \left(\frac{p_{H_2}}{p_{ref}}\right)\left(\frac{p_{H_2O}}{p_{ref}}\right) e^{\frac{-E_{act,a}}{RT}} \quad (3.33)$$

$$i_c = i_{o,cat}\left(e^{-\beta\eta F/RT} - e^{(1-\beta)\eta F/RT}\right) \quad (3.34)$$

$$i_{o,cat} = \gamma_c \left(\frac{p_{O_2}}{p_{ref}}\right)^{0.25} \exp^{\frac{-E_{act,c}}{RT}} \quad (3.35)$$

3.2.5. Boundary conditions

The boundary conditions for the fuel in the flow channel are given in Table 3.2. At the flow channel/ electrode interface ($0 < x < x_a$, $y = y_e$), transport by shear stresses is zero, meaning there is no force across the boundary. Furthermore, at this boundary, a continuity of mass and heat is assumed. The boundary conditions of the air flow in the air flow channel as found in Table 3.3 are similar to those of the fuel flow, apart from the gas components and initial concentration.

In Table 3.4, at the electrode/electrolyte interface, electrochemical reactions are assumed; oxidation reaction occurs on the anode/electrolyte interface and reduction reaction on the cathode/electrolyte interface. Oxidation reaction is assumed as a boundary condition in the vicinity of the anode/ electrolyte where the mass sink/source and heat source are determined. In the mean time, reduction reaction of O_2 is assumed at the cathode/ electrolyte interface with the mass sink.

Table 3.2. Boundary conditions of the fuel flow channel

Equations	x = 0, $y_e < y < y_f$	$0 < x < x_a$, y = y_e	$0 < x < x_a$, y = y_f	x = x_a, $y_e < y < y_f$
Mass and momentum	$\mathbf{u}\cdot\mathbf{n} = u_a$	$\eta(\nabla u + (\nabla u)^T)\, n = 0$	u = 0, $\mathbf{n}\cdot(q_1-q_2) = 0$;	$\mathbf{u}\cdot\mathbf{t} = 0$, $p = p_0$
Energy	$T = T_0$	$\mathbf{n}\cdot(q_1-q_2) = 0$; $q_i = -k_i\nabla T_i + \rho_i C_{pi} T_i u_i$	$q_i = -k_i\nabla T_i + \rho_i C_{pi} T_i u_i$	$\mathbf{n}\cdot q = 0$
Gas species	$c_i = c_{i,0}$, i = CH_4, H_2O, CO, H_2, CO_2	$\mathbf{n}\cdot(N_1 - N_2) = 0$; $N_i = -D_i\nabla c_i + c_i u_i$	$\mathbf{n}\cdot N = 0$; $N_i = -D_i\nabla c_i + c_i u_i$	$q = -k\nabla T$; $\mathbf{n}\cdot N = 0$; $N = -D\nabla c_i$

Table 3.3. Boundary conditions of the air flow channel

Equations	x = 0, $y_a < y < y_b$	$0 < x < x_a$, y = y_a	$0 < x < x_a$, y = y_b	x = x_a, $y_a < y < y_b$
Mass and momentum	$\mathbf{u}\cdot\mathbf{n} = u_c$	u = 0	$\eta(\nabla u + (\nabla u)^T)\, n = 0$	$\mathbf{u}\cdot\mathbf{t} = 0$, $p = p_0$
Energy	$T = T_0$	$\mathbf{n}\cdot(q_1-q_2) = 0$; $q_i = -k_i\nabla T_i + \rho_i C_{pi} T_i u_i$	$\mathbf{n}\cdot(q_1-q_2) = 0$; $q_i = -k_i\nabla T_i + \rho_i C_{pi} T_i u_i$	$\mathbf{n}\cdot q = 0$; $q = -k\nabla T$
Gas species	$c_j = c_{j,0}$, j = O_2, N_2	$\mathbf{n}\cdot N = 0$; $N_i = -D_i\nabla c_i + c_i u_i$	$\mathbf{n}\cdot(N_1 - N_2) = 0$; $N_i = -D_i\nabla c_i + c_i u_i$	$\mathbf{n}\cdot N = 0$; $N = -D\nabla c_i$

Table 3.4. Boundary conditions at the electrodes/electrolyte interface

Equations	$0 < x < x_a$, y = y_c	$0 < x < x_a$, y = y_d	All others
Mass and momentum	u = 0	u = 0	u = 0
Energy	$\mathbf{n}\cdot(q_1-q_2) = 0$; $q_i = -k_i\nabla T_i + \rho_i C_{pi} T_i u_i$	$\mathbf{n}\cdot(q_1-q_2) = q_0$; $q_i = -k_i\nabla T_i + \rho_i C_{pi} T_i u_i$; $q_0 = (\frac{-\Delta H_{ox}}{2F} \times i) - (i \times v_{cell})$	$\mathbf{n}\cdot q = 0$; $q_i = -k\nabla T + \rho C_p T u$
Gas species	$\mathbf{n}\cdot(N_1 - N_2) = N_0$; $N_i = -D_i\nabla c_i + c_i u_i$; $\mathbf{N}_0 = -\frac{i}{4F}$	$\mathbf{n}\cdot(N_1 - N_2) = N_0$; $N_i = -D_i\nabla c_i + c_i u_i$ $\mathbf{N}_{0,H_2} = -\frac{i}{2F}$, $\mathbf{N}_{0,H_2O} = \frac{i}{2F}$	$\mathbf{n}\cdot N = 0$; $N = -D\nabla c + cu$

Boundary conditions for electronic and ionic charge equations for electrodes and electrolyte are given in Table 3.5. For ionic charge transport, at the anode/electrolyte ($0 < x < x_a, y = y_d$) interface, the normal ionic current density is equal to i_a which is determined to be a positive value as the positive current flow into the electrolyte from the anode. Consequently, at the cathode/electrolyte interface ($0 < x < x_a, y = y_c$), the normal ionic current density has the same magnitude as i_c but with the negative sign since the current enters the cathode from the electrolyte. For the electronic charge transport, since the ionic and electronic charges flow in the opposite direction, the opposite signs of i_a and i_c from those of ionic charge transport at the interfaces are assumed. It is noted that the values of some boundary conditions and other constant values are provided in Table. 3.6.

Table 3.5. Boundary conditions for electronic and ionic charge equations for electrodes and electrolyte domains

	$0 < x < x_a$, $y = y_b$	$0 < x < x_a$, $y = y_c$	$0 < x < x_a$, $y = y_d$	$0 < x < x_a$, $y = y_e$	All others
Electronic charge	$\phi_s = 0$	$-\mathbf{n}\cdot\mathbf{J} = i_c$	$-\mathbf{n}\cdot\mathbf{J} = -i_a$	$\phi_s = -v$	$\mathbf{n}\cdot\mathbf{J} = 0$
Ionic charge	-	$-\mathbf{n}\cdot\mathbf{J} = -i_c$	$-\mathbf{n}\cdot\mathbf{J} = i_a$	-	$\mathbf{n}\cdot\mathbf{J} = 0$

Table 3.6. Initial and operating conditions

Parameters	Description
Fuel inlet concentration, $c_{i,o}$	CH_4 17.1%, H_2O 49.3%, H_2 26.3%, CO 2.9% and CO_2 4.4%
Operating pressure, p_o	101300 Pa
Operating voltage, v	0.7 V
Inlet temperature, T_o	1123 K
Fuel inlet velocity, u_a	2 m/s
Air inlet velocity, u_c	2 m/s
$E_{act,a}$	100 kJ/mol
$E_{act,c}$	120 kJ/mol
γ_a	5.5×10^8 A/m^2
γ_c	7×10^8 A/m^2

3.2.6. Numerical implementation

The governing equations equipped with kinetic equations of the steam reforming, water-gas shift and electrochemical reactions are solved using COMSOL Multiphysics 3.5 based on the Finite Element Method technique. Structured mesh elements compose of 2D rectangles with 1000 elements contained in the computational domain. A stationary nonlinear solver

with direct linear system solver (SPOOLES) is used for a non-linear problem with the relative tolerance of 1×10^{-6}.

3.3. Results and discussions

The SOFC model has been initially developed under an assumption that the inlet fuel gas is 30% pre-reformed [1, 3] as the gas composition is shown in Table 3.6. Apart from the electrochemical reaction, the steam reforming reaction and the water-gas shift reaction are taken place in the anode compartment.

Fig. 3.2 shows the good agreement between the current density and the operating voltage obtained by the present study and the current density and the operating voltage of the experimental data available in Kim et al. [29]. In the work of Kim et al [29], the anode-supported flat-tube SOFC with the anode porosity of 0.5 was developed. The cell area of 23 cm^2 was tested at the temperature of 1023 K. The discrepancy found in Fig. 3.2 might have been caused by the difference in operating temperature (100 K) and the model parameters that do not correspond to those of the experiments.

Fig. 3.3 describes the variation of the rate of reforming reaction along the porous anode depth at the distance of 0.005 m from the anode channel entrance. It can be observed that the rate of reforming reaction is high near the surface of the porous anode and rapidly reduced afterwards. In addition, it has been observed that an increase in the porosity also enhances the rate of reforming reaction. This is because the rate of reforming reaction is highly dependent on CH_4 partial pressure. Although an increase in the porosity yields the decreasing reactive surface area (A_v) which should result in the lower rate of reforming reaction according to Eq. (3.19), the rate of reforming reaction is rather dominated by the effective diffusivity of CH_4 and permeability which allow the higher amount of CH_4 to penetrate into the porous anode and consequently, the higher rate of reforming reaction occurs. It is noted that the radii of the electron conduction particles and the ion conducting particles are fixed at 0.1 μm. Therefore, an increase in porosity provides the increasing void fraction and decreasing reactive surface area.

The rate of shift reaction is increased with the increase of anode porosity according to Fig. 3.4. An increase in porosity provides higher effective diffusivity and permeability of gases, and, consequently, the rate of shift reaction.

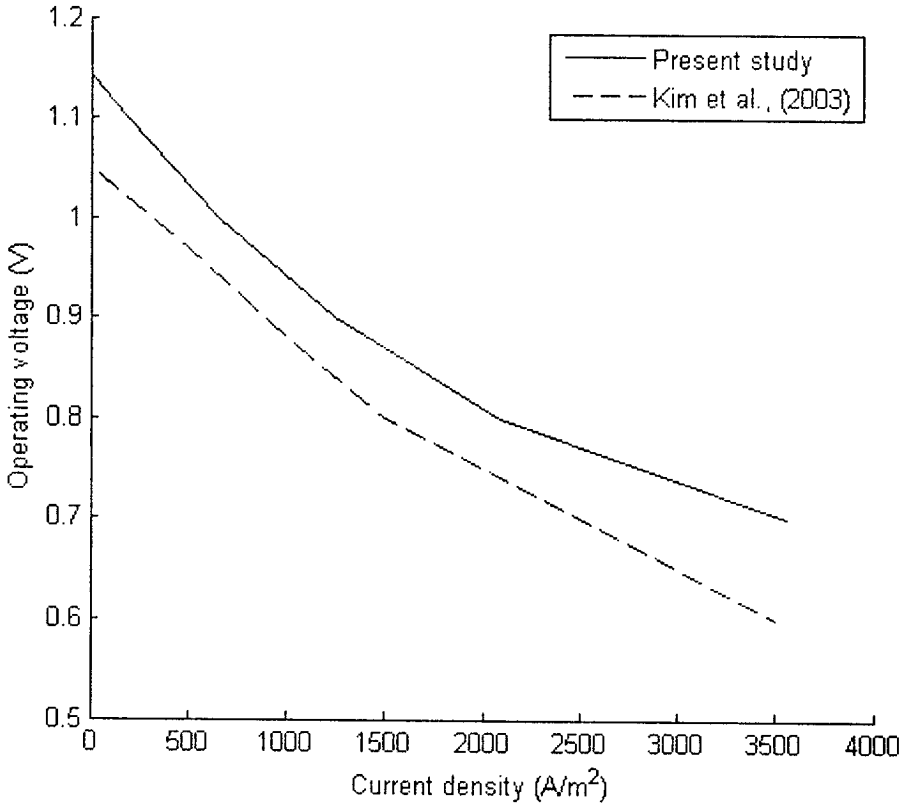

Figure 3.2. I-V characteristics of the anode-supported SOFC

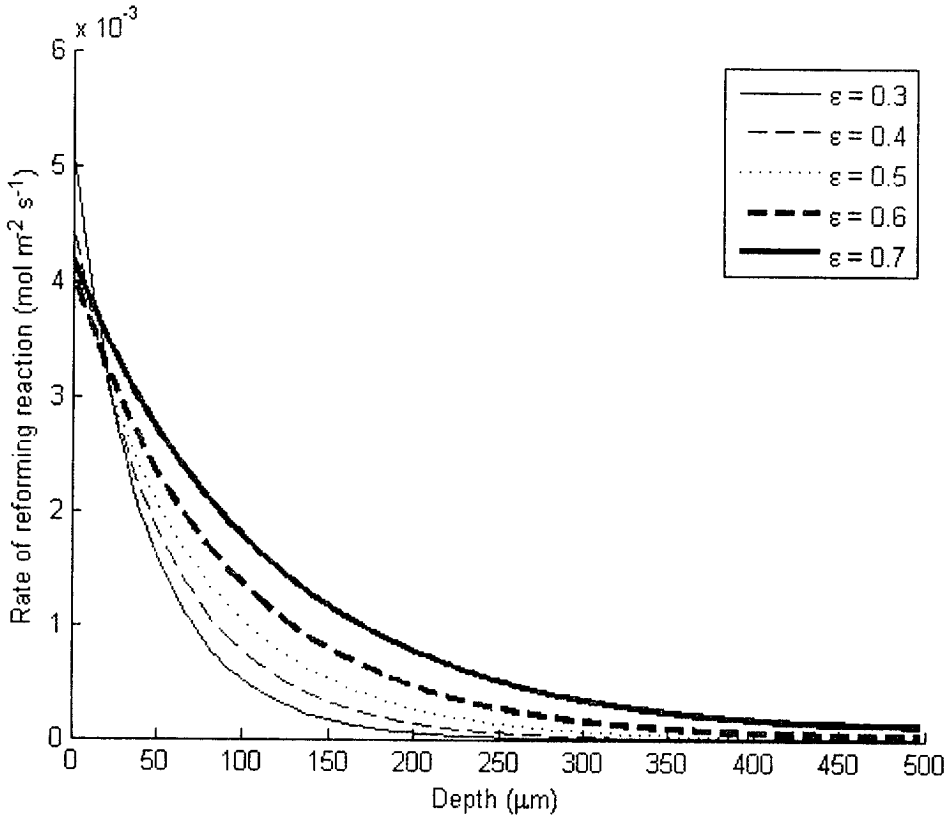

Figure 3.3. Rate of reforming reaction along the anode depth

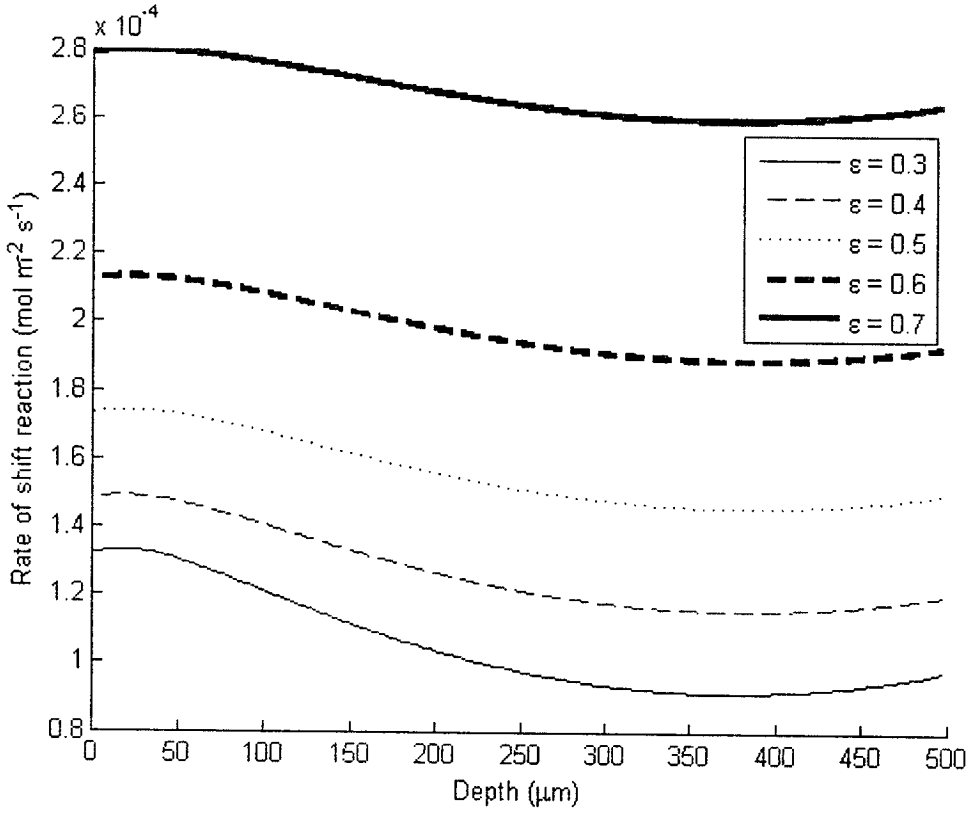

Figure 3.4. Rate of shift reaction along the anode depth

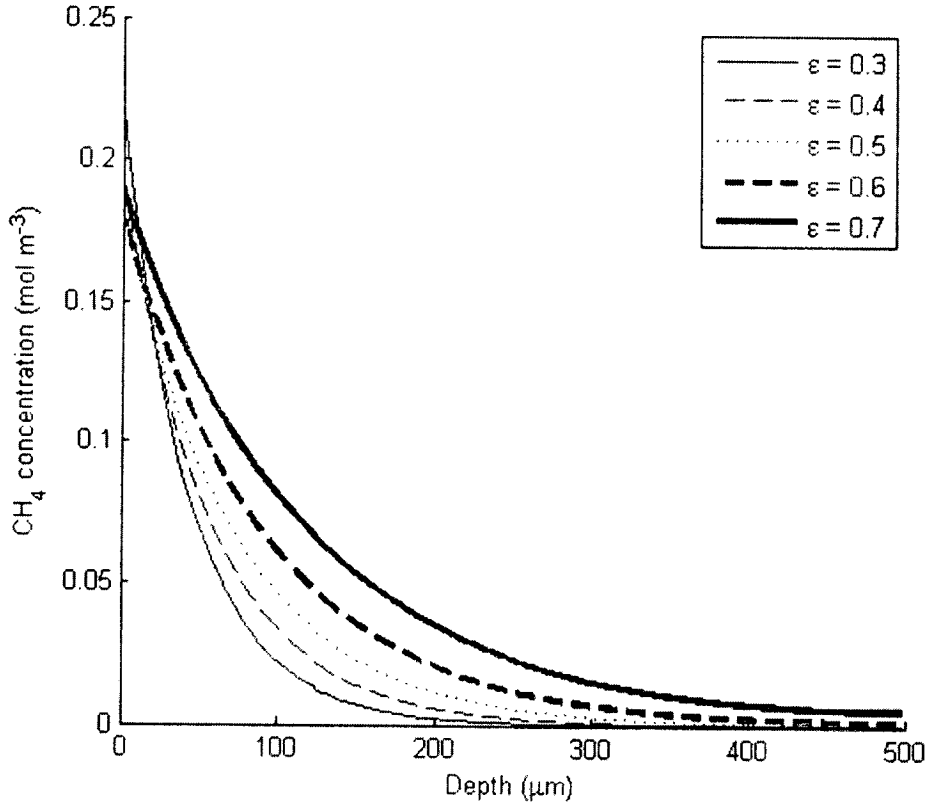

Figure 3.5. CH_4 concentration along the anode depth

Fig. 3.5 shows the effect of anode porosity on CH_4 concentration along the anode depth at the distance of 0.005 m from the anode channel entrance. It can be seen that at the same depth of porous anode, CH_4 is increased with an increase in porosity. This is due to the fact that an increase in the porosity increases the void fraction, effective diffusivity coefficient and permeability, facilitating a larger amount of CH_4 to diffuse to anode/electrolyte surface.

H_2O content along the depth of the porous anode at the distance of 0.005 m from the anode channel entrance is plotted in Fig. 3.6. H_2O is gradually reduced and subsequently escalated as it is consumed in the steam reforming reaction and produced by electrochemical reaction. With an increasing depth, it can be seen that enhancing the anode porosity yields the lower H_2O content in the porous anode. The higher anode porosity exhibits the lower reactive surface area and electrical resistance of the porous anode structure as expressed in Eq. (3.8). According to those effects, the current density produced is consequently lower and H_2O produced is less.

Fig. 3.7 illustrates H_2 content along the depth of the porous anode at the distance of 0.005 m from the anode channel entrance. H_2 content is considerably raised near the anode surface due to its high rate of steam reforming reaction and shift reaction near the surface. Meanwhile, H_2 is also consumed by the electrochemical reaction making its content gradually decline.

When focusing on the H_2 production, the hydrogen production rate depends significantly on the rate of reforming reaction rather than the rate of shift reaction according to Eq.(3.25). As a result, with the increasing anode porosity, the rate of reforming reaction is increased as well as H_2 content along the anode depth. However, it can be seen from Fig. 3.6 that the production of H_2 with the anode porosity of 0.6 and 0.7 are lower than expected. This is due to the fact that the anode reactive surface area is decreased against the increasing porosity. Therefore, the decrease in the specific anode area partly dominates the H_2 production, resulting in the less H_2 concentration at the porosity of 0.6 and 0 .7. In terms of H_2 consumption by the electrochemical reaction, an increase in anode porosity provides a higher effective diffusivity of H_2 and permeability; however, it also gives the lower reactive surface area and the effective electrical conductivity. Consequently, consumption of H_2 by the electrochemical reaction is reduced with an increase in anode porosity as it is illustrated in Fig. 3.7.

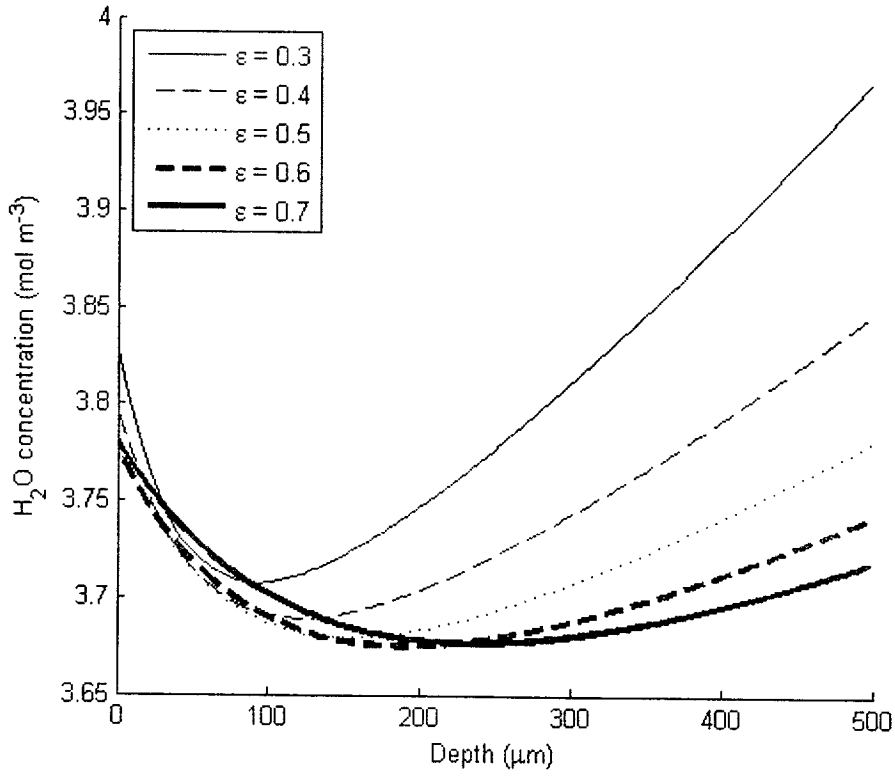

Figure 3.6. H_2O content along the anode depth

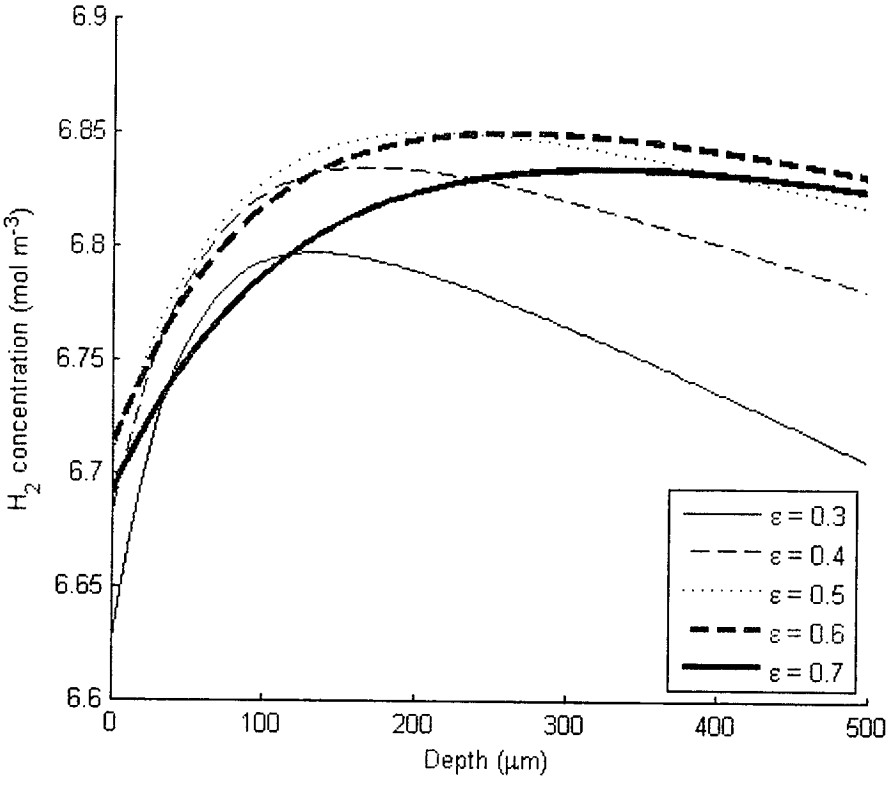

Figure 3.7. Mass concentration (mol/m^3) of H_2 in the anode flow channel

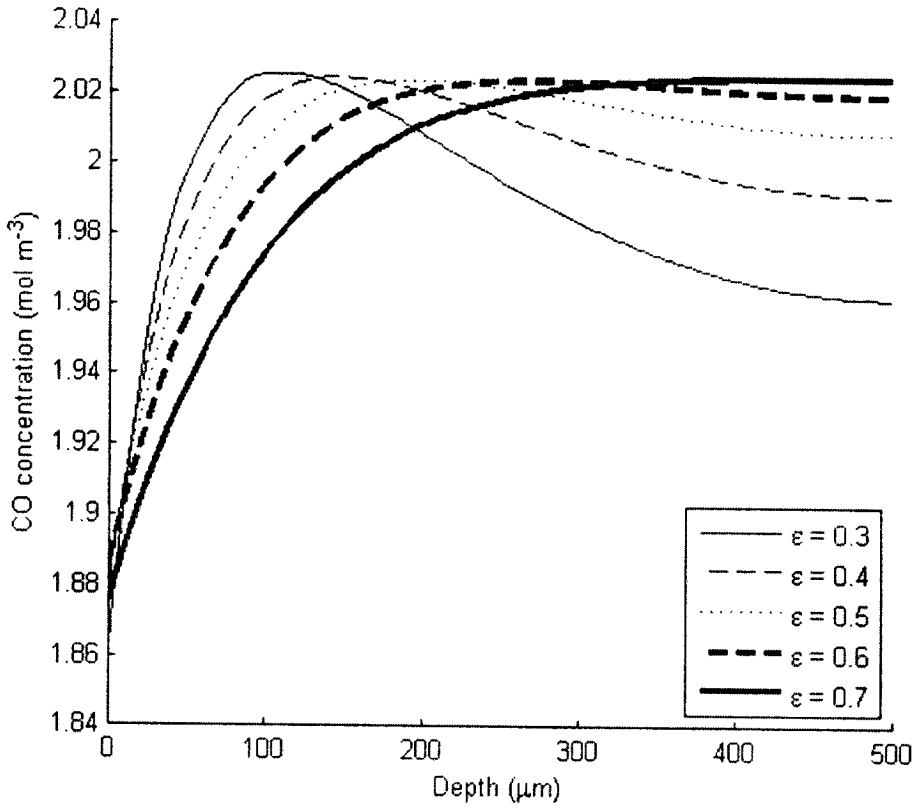

Figure 3.8. Mass concentration (mol/m^3) of CO in the anode flow channel

CO is generated by the reforming reaction and it is shifted into H_2 and CO_2 by the shift reaction. This is illustrated in Fig. 3.8 in that, in the vicinity of the anode surface, the amount of CO is rapidly increased and then gradually decreased due to the reforming reaction and the shift reaction, respectively. With an increase in the anode porosity, the decreasing reactive surface area dominates over the increasing rate of reforming reaction, leading to the decreasing amount of CO production in the beginning. Subsequently, CO reacts with H_2O generating CO_2 and H_2. As depicted in Figs. 3.6 and 3.8, both CO and H_2O contents are the greatest near the surface at the anode porosity of 0.3, promoting the shift reaction to propagate and the CO content is reduced massively.

As aforementioned, it has been found from Fig. 3.7 that CO content at the lower anode porosity is consumed by the shift reaction more than that at the higher anode porosity. Therefore, as seen in Fig. 3.9, CO_2 production is higher at lower anode porosity and it is decreased with the increasing anode porosity.

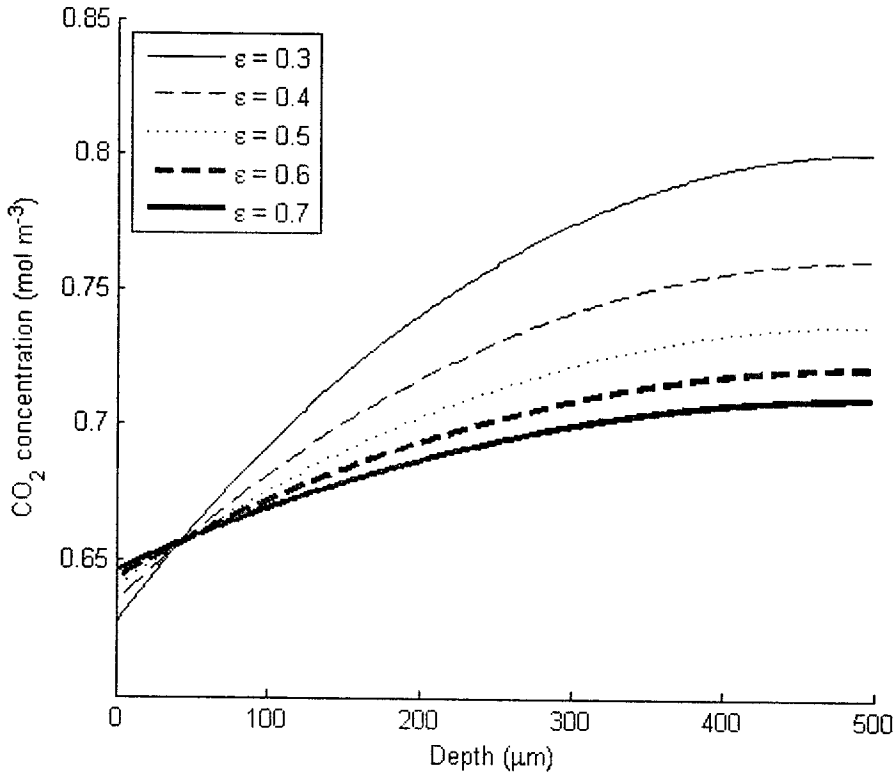

Figure 3.9. Mass concentration (mol/m^3) of CO_2 in the anode flow channel.

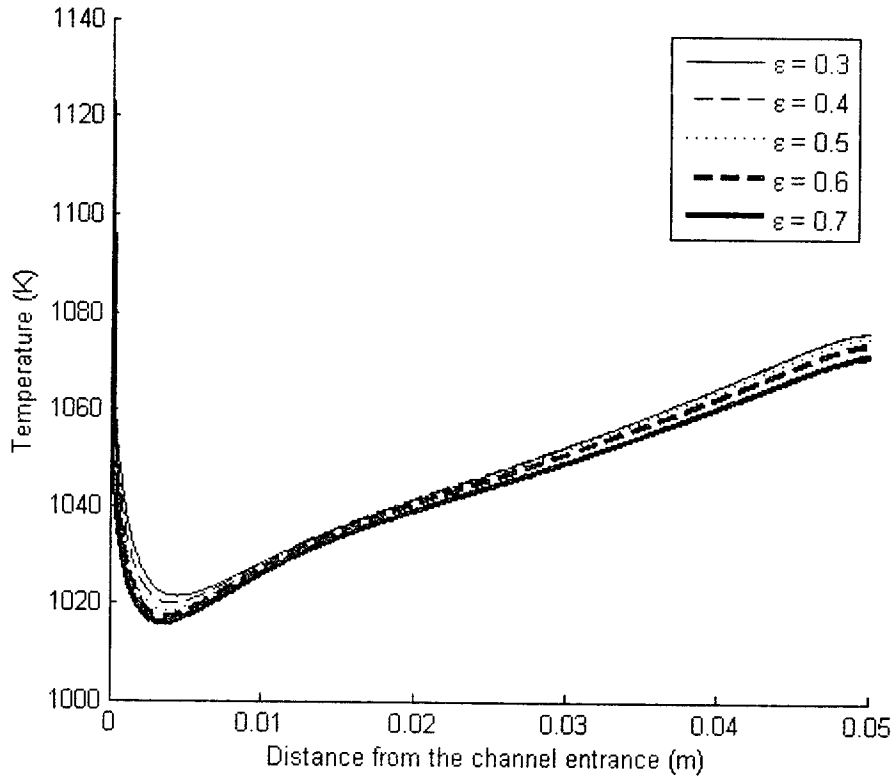

Figure 3.10. The temperature variation along the porous anode surface

Since the temperature along the anode depth for each porosity does not show an obvious variation and endothermic and exothermic reactions are involved in the anode side, the temperature distribution along the porous anode channel is essential. Fig. 3.10 shows the temperature variation along the porous anode surface. The channel entrance starts at 0 m. Since the reforming reaction is highly endothermic, the temperature is significantly reduced near the channel entrance where the high rate of reforming is found. The temperature is then gradually increased by heat generated from shift and oxidation reactions. By increasing the anode porosity, the temperature at the anode surface is slightly decreased. Even though the rate of reforming reaction is increased with the increase of porosity, the decreasing reactive surface area dominates over the increasing rate of reaction, leading to the decrease of the heat generated.

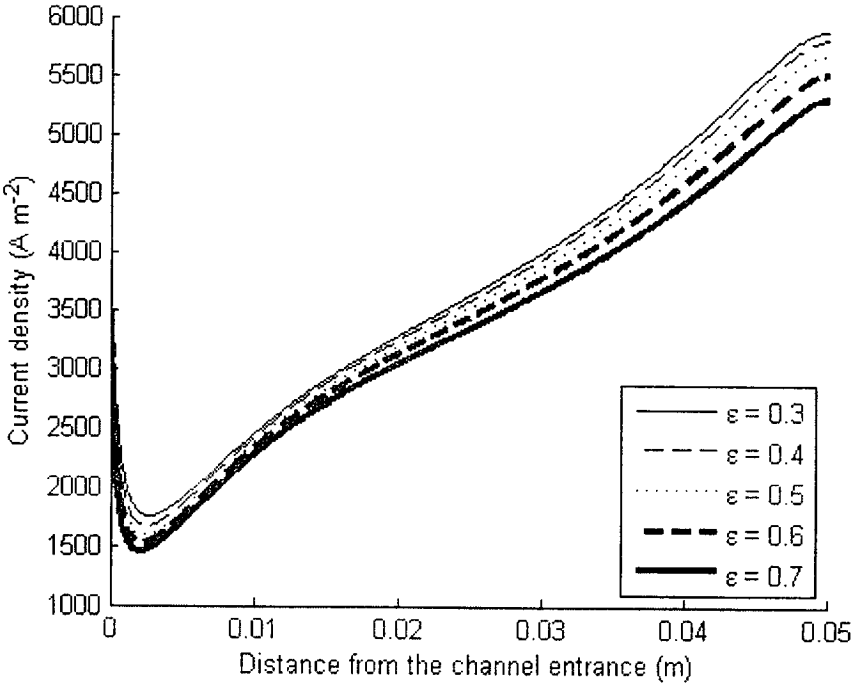

Figure 3.11. The current density variation along porous anode/electrolyte interface

Accordingly, the current density along the anode/electrolyte interface is plotted in Fig. 3.11. It can be seen that the current density variation behaves similarly to the temperature variation as illustrated in Fig. 3.9. This is because the current density is dependent on the temperature Therefore, the current density is massively reduced near the channel entrance where the rate of reforming is raised steeply and the temperature is extremely diminished. It is also found that the higher anode porosity causes the lower current density. This is due to the fact that, by increasing the porosity, the reactive surface area is less resulting in the reduction of current density.

4. Transient analysis of Solid Oxide Fuel Cell during start-up period

4.1. Introduction

In order to obtain a better understanding of the SOFC operation, a number of theoretical models have been developed. Some studies have modelled SOFC in various SOFC conditions [5-9] Nevertheless, there are few investigations taking the influences of anode flow feeding. Since SOFC operates at high temperature (800 - 1000 C), a sudden change of parameters such as fuel flow velocity and temperature will have effects to the rate of reaction and, subsequently, a large temperature difference leads to substantial thermomechanical stress. In the present study, such work will be conducted by the model developed for planar anode-supported SOFC with internal methane steam reforming reaction based on a certain steam to carbon ratio. The one and two step change of input parameters will be investigated and results will be further discussed.

4.2. Model Development

The two-dimensional model has been developed for the anode-supported planar SOFC. The conservation of mass, momentum and energy are taken into account including the conservation of charge, and kinetics of electrochemical and chemical reactions. The details of the mathematical modelling are presented as follows:

4.2.1. Geometry, properties and assumptions

The cell has been designed involving "ribbed" channels which act as both current collectors and flow directors. The 1 mm high and 50 mm long anode and cathode flow channels have been developed in this work according to Figure 1. Further details of dimensions and physical properties are given in Table 4.1 [22].

Table 4.1. Dimensions and physical properties of cell components.

Material	Thickness (μm)	Density (kg/m^3)	Conductivity (W/mK)	Specific heat (J/kgK)
Electrolyte	20	5900	2	550
Anode	500	6950	3	400
Cathode	50	6580	3	300
Interconnect	500	6600	3.5	400

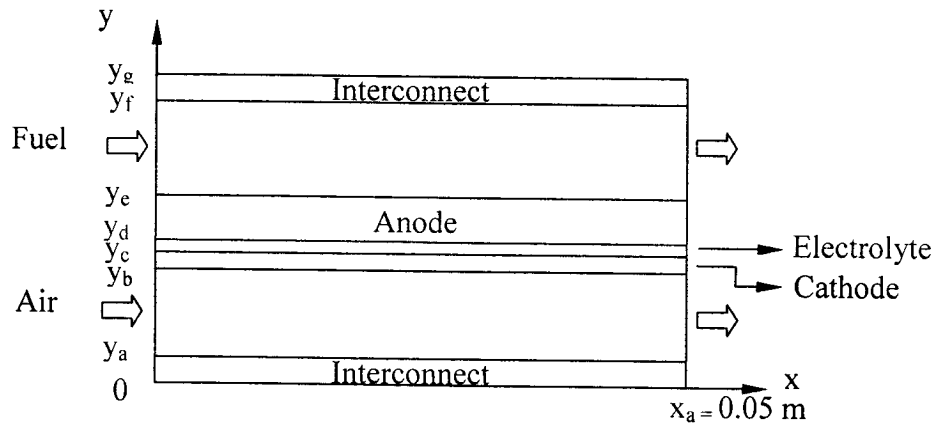

Figure 4.1. Schematic diagram of a fuel cell model.

This mathematical modelling has been developed based on assumptions as follows:

(1) The model is based on two-dimensional flow under transient condition.

(2) The reactant gas mixtures are ideal gases.

(3) Gas flow in the channel is laminar.

(4) Incompressible flow is assumed.

(5) Radiative heat transfer is negligible.

4.2.2. Transport equations

In this model, the governing equations of mass, momentum and energy including the charge conservation are applied to the computational domain to calculate the concentration, velocity, temperature and potential profiles within the domain. The governing equations are consequently solved by the Computational Fluid Dynamics (CFD) technique through Eqs. (4.1-4.3).

Conservation of mass:

$$\nabla \cdot u = 0 \tag{4.1}$$

Conservation of momentum:

$$\rho \frac{\partial u}{\partial t} + \rho u \cdot \nabla u + \nabla p - \nabla \cdot \left[\mu \left(\nabla u + (\nabla u)^T \right) \right] = 0 \tag{4.2}$$

Conservation of energy:

$$\rho C_p \frac{\partial T}{\partial t} + \nabla \cdot \left(-k \nabla T + \rho C_p T u \right) = Q \tag{4.3}$$

Convection and diffusion of various gas species in the flow channel must be involved in the computational domain, thus the conservation of mass species can be expressed in Eq.(4.4) as

$$\frac{\partial c_i}{\partial t} + \nabla \cdot \left(-D_i \nabla c_i + c_i u \right) = R_i \tag{4.4}$$

Conservation of charge:

The ionic charge conservation equation is applied to the electrolyte layer according to Eq.(4.5).

$$-\nabla\cdot\left(\sigma_e\nabla\phi_e\right) = 0 \tag{4.5}$$

and σ_e can be defined in Eq. (4.6) as

$$\sigma_e = \frac{1}{3\times10^{-5}\exp(10300/T)} \tag{4.6}$$

The electronic charge conservation equation as expressed in Eq.(4.7) is applied to both cathode and anode

$$-\nabla\cdot\left(\sigma_s\nabla\phi_s\right) = 0 \tag{4.7}$$

with the expression of σ_s as shown in Eq. (8)

anode:
$$\sigma_s = \frac{1}{2.98\times10^{-5}\exp(-1392/T)}\times\frac{(1-\varepsilon)}{\tau} \tag{4.8}$$

When the calculation domains are both anode and cathode, the conservation of momentum is expressed by Eq. (4.9).

$$\rho\frac{\partial u}{\partial t}+\nabla p-\nabla\cdot\left[\mu\left(\nabla u+(\nabla u)^T\right)\right]=-\frac{\mu}{k_p}u \tag{4.9}$$

and k_p is defined in Eq. (4.10) [17] as

$$k_p = \frac{\varepsilon^3}{180(1-\varepsilon)^2}d_p^2 \tag{4.10}$$

D_i is the effective mass diffusivity of component i in the porous media as expressed in other work [4,25].

In addition, the effective thermal conductivity (k_{eff}) as shown in Eq. (4.11) [11, 21] will be used in Eq. (3) when energy conservation in electrodes is considered.

$$k_{eff} = (1-\varepsilon)k_s + \varepsilon k_g \tag{4.11}$$

4.2.3. Chemical reactions

Due to the fact that methane (CH_4) can be reformed and shifted into hydrogen (H_2) through steam reforming and water-gas shift reactions as shown in Eqs. (4.12) and (4.14), the rate of the steam reforming reaction and the water-gas shift reaction are also considered in the anode domain as shown in Eqs. (4.13) and (4.15), respectively.

Steam reforming reaction: $CH_4 + H_2O \rightarrow 3H_2 + CO$ (4.12)

Rate of steam reforming reaction [10]: $R_r = k_o p_{CH_4} e^{(-E_a/(RT))} \times A_v$ (4.13)

Water-gas shift reaction: $CO + H_2O \rightarrow CO_2 + H_2$ (4.14)

Rate of water-gas shift reaction [2, 3, 11]: $R_s = k_{wgs} p_{H_2O} p_{CO}\left(1-\frac{p_{H_2}p_{CO_2}}{p_{H_2O}p_{CO}K_{s,eq}}\right)$ (4.15)

Finally, the rate of production of gas species can be formulated as shown in Eqs. (4.16) - (4.20) [3,18]:

$$R_{CH_4} = -R_r \quad (4.16)$$

$$R_{CO} = -R_r - R_s \quad (4.17)$$

$$R_{H_2O} = -R_r - R_s \quad (4.18)$$

$$R_{H_2} = 3R_r + R_s \quad (4.19)$$

$$R_{CO_2} = R_s \quad (4.20)$$

Heat source term, Q (W m^{-3}), in Eq. (4.3) can be defined according to the heat of reaction of the steam reforming reaction and the water-gas shift reaction as shown in Eqs. (4.21). In addition, there is also a heat source term at the anode/electrolyte interface due to the emerging of oxidation reaction as expressed in Eqs. (4.22) and (4.23).

$$Q = (R_r \times \Delta H_r \times A_v) + (R_s \times \Delta H_s) \quad (4.21)$$

where enthalpy of formation of reforming reaction (ΔH_r) is 206 × 10^3 J mol^{-1} and enthalpy of formation of shift reaction (ΔH_s) is -41.1 × 10^3 J mol^{-1}.

$$Q_{ox} = \left(\frac{-\Delta H_{ox}}{2F} \times i\right) - (i \times v_{cell}) \quad (4.22)$$

Enthalpy of oxidation reaction (J mol^{-1}): $\Delta H_{OX} = -(240506 + 7.3835T)$ (4.23)

4.2.4. Electrochemical reactions

At three phase boundary on the anode side, hydrogen gas reacts with oxygen ions, producing water and electrons. Electrons flow from the anode to the cathode through the external circuits and react with oxygen gas, giving oxygen ions. Consequently the electric current is produced as shown in Eqs. (4.24) – (4.25). The overall reaction expressed in Eq. (4.26) is assumed as a boundary condition in the vicinity of the electrolyte/anode interphase where the mass sink and source are determined in Eqs. (4.27) to (4.29).

Anode: $$H_2 + O^{2-} \rightarrow H_2O + 2e^- \quad (4.24)$$

Cathode: $$\frac{1}{2}O_2 + 2e^- \rightarrow O^{2-} \quad (4.25)$$

Overall reaction: $$H_2 + \frac{1}{2}O_2 \rightarrow H_2O + Electricity + Heat \quad (4.26)$$

H_2 consumption: $$S_{H_2} = -\frac{i_a}{2F} \quad (4.27)$$

O_2 consumption: $$S_{O_2} = -\frac{i_c}{4F} \quad (4.28)$$

H_2O production: $$S_{H_2O} = -\frac{i_a}{2F} \quad (4.29)$$

Anodic current density (i_a) and anodic exchange current density ($i_{o,an}$) can be defined as Eqs. (4.30) [27] and (4.31) [28] as well as cathodic current density (i_c) and cathodic exchange current density ($i_{o,cat}$) in Eqs. (4.32) [27] and (4.33) [28]

$$i_a = i_{o,an}\left(e^{(1-\beta)\eta F/RT} - e^{-\beta\eta F/RT}\right) \quad (30)$$

$$i_{o,an} = \gamma_a \left(\frac{p_{H_2}}{p_{ref}}\right)\left(\frac{p_{H_2O}}{p_{ref}}\right) e^{\frac{-E_{act,a}}{RT}} \quad (31)$$

where $E_{act,a}$ is equal to 100 kJ mol^{-1} and pre-exponential factor ($\square_a$) is 5.5×10^8 A m^{-2}.

$$i_c = i_{o,cat}\left(e^{-\beta\eta F/RT} - e^{(1-\beta)\eta F/RT}\right) \quad (4.32)$$

$$i_{o,cat} = \gamma_c \left(\frac{p_{O_2}}{p_{ref}}\right)^{0.25} \exp^{\frac{-E_{act,c}}{RT}} \quad (4.33)$$

where $E_{act,c}$ is equal to and 120 kJ mol^{-1} and γ_c is equal to 7×10^8 A m^{-2}.

4.2.5. Boundary conditions

It is assumed that the steam reforming and water-gas shift reaction are occurred on the anode surface whereas the oxidation reaction is assumed at the anode/electrolyte interphase. At this interphase, mass source and sink due to the oxidation reaction as expressed in Eqs. (4.27) and (4.29) are applied. Reduction reaction is assumed at the cathode/electrolyte enterphase where mass sink is expressed in Eq. (4.28). Heat source due to steam reforming, water-gas shift and oxidation reactions as expressed in Eqs. (4.21) and (4.22) is applied at the anode/electrolyte interphase. At the channel outlet, the normal flow and convection are assumed.

4.2.6. Numerical implementation

The governing equations equipped with kinetic equations of the steam reforming, water-gas shift and electrochemical reactions are solved using COMSOL Multiphysics 3.5 based on the Finite Element Method technique. Structured mesh elements compose of 2D rectangles with 1000 elements contained in the computational domain. Sensitivity analysis has been performed and insured. However, it is noted that grids are uniform in x direction and non-uniform in y direction due to the very thin electrolyte and cathode used in the model. Since charge transfer is not affected significantly by time scale unlike those of heat and mass transfer, charge conservation equations are then soled under steady-state condition where a stationary nonlinear solver with direct linear system solver (SPOOLES) is used for a non-linear problem with the relative tolerance of 1×10^{-6}. For transient problems, some operating parameter disturbances are imposed and the time intervals chosen are as small as 10^{-5} s near those step changes. Mass, momentum and energy conservation equations are solved by SPOOLE system solver.

4.3. Results and discussions

An SOFC unit model is developed where the transient problem without imposed parameters of a co-flow SOFC unit is analysed in section 3.1 as the base case. It is then compared with the transient condition with step changes of inlet velocity and temperature as discussed in sections 3.2 and 3.3, respectively.

Table 4.2. Initial and operating conditions

Parameters	Description
Fuel inlet mole fraction, $y_{i,o}$	CH_4 33%, H_2O 67%
Operating pressure, p_o	101300 Pa
Operating voltage, v	0.7 V

4.3.1. Analysis of transient condition of base case

The base case, considered as case A, is simulated to observe the transient behaviour of the cell when there is no disturbance applied. Fuel and air inlet velocity are considered at 2 m s^{-1} and both inlet fuel and air temperature are maintained at 1123 K. Other input fuel and air conditions are indicated in Table 4.2.

Concentration of gases on the anode surface at x = 0.01 m are plotted against time as illustrated in Figure 4.2. Since the distance of x = 0.01 m is in the vicinity of the channel entrance, it can be observed that CH_4 concentration is gradually raised from zero even though it is highly consumed by the steam reforming reaction near the entrance. During 0 to 1 s, H_2O is substantially increased as H_2O is freshly fed into the flow channel. It is then consumed by the steam reforming and water-gas shift reactions and produced by the electrochemical reaction occurred on the anode side. Therefore, there is a drop of H_2O at the beginning and it is subsequently increased until it reaches the steady state. CO and H_2 is produced by the steam reforming reaction. This reaction takes place immediately as CH_4 and H_2O enter the flow channel so that the concentration of CO and H_2 is considerably increased during 0 to 1 s. Afterwards, there is a drop of CO concentration before entering the steady state as it is converted into H_2 and CO_2 by the water-gas shift reaction. At the same time, a drop of H_2 concentration indicates that H_2 is consumed by the electrochemical reaction on the anode side before reaching its steady state at 125 s approximately.

Plots of anode surface temperature against time can be illustrated in Figure 4.3 at different locations (x) along the anode surface. At x = 0.005 and 0.01 m, the temperature is declined rapidly since the strongly endothermic steam reforming reaction occurs rapidly near the channel entrance. Heat produced by the water-gas shift and electrochemical reactions makes a boost of anode temperature as found in the plots of temperature at x = 0.02 to

0.05 m. As time proceeds, gases and heat flow towards the exit of the channel and the effect of the strongly endothermic reaction spreads widely, making a rapid decrease of temperature over the entire anode surface. It has been found that anode surface temperature ranges from 853 to 1208 K, equal to the temperature difference of 355 K. It takes 185 s for the temperature to reach its steady state.

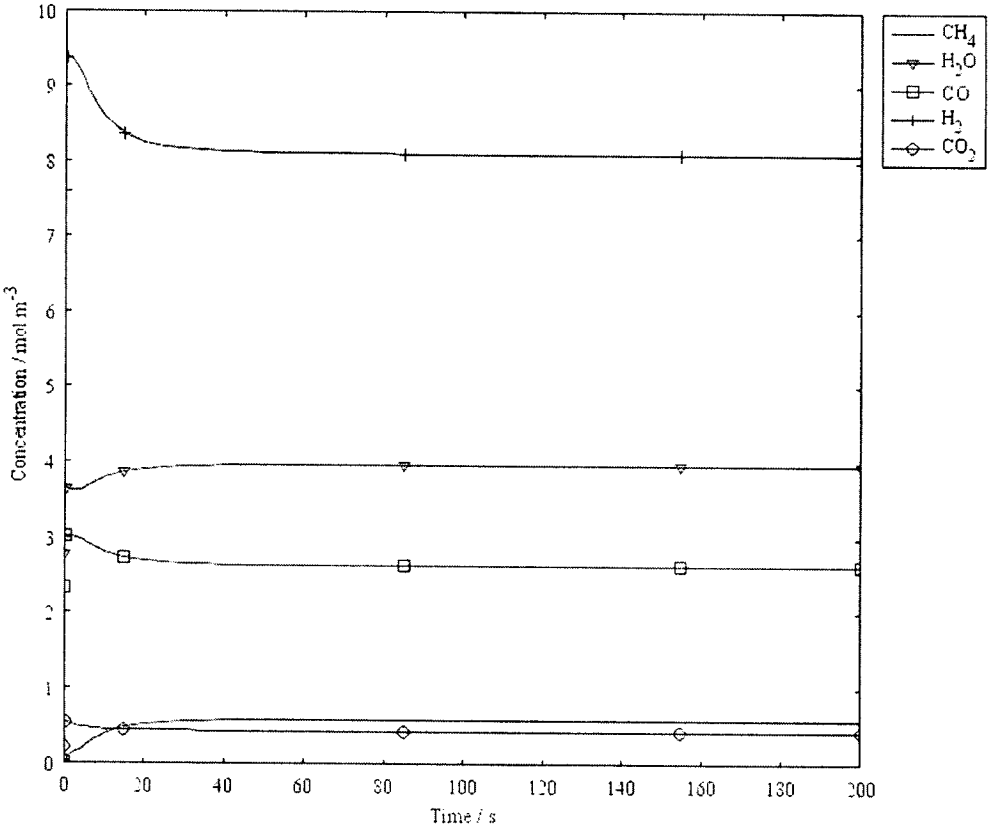

Figure 4.2. Concentration profiles of gases in case A against time at x = 0.01 m.

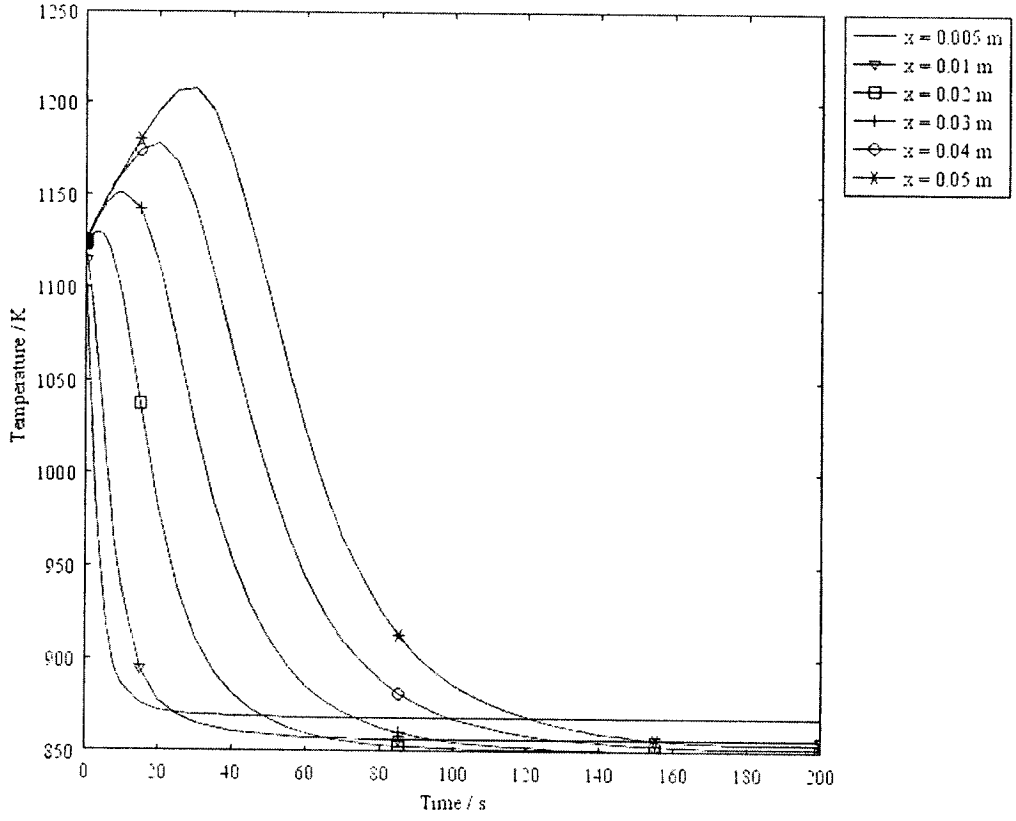

Figure 4.3. Temperature profiles of case A against time

4.3.2. Analysis of transient condition with step change of inlet velocity

In this section, the transient behaviour of the SOFC have been investigated through cases B and C due to step changes of inlet velocity at the entrance of the fuel channel. In case B, the inlet fuel velocity is initially set at 1 m s^{-1} then it is jumped from 1 to 2 m s^{-1} at 1 s. Other parameters are kept constant and initial and operating conditions are determined as shown in Table 4.2. In case C, a model with two step change of inlet velocity from 1 to 1.5 m s^{-1} at 1 s and from 1.5 to 2 m s^{-1} at 5 s is investigated. The results of cases B and C are discussed and compared with those of case A.

Gas concentration along the anode surface is plotted against time as depicted in Figure 4.4. In case B, the fuel inlet velocity is jumped from 1 to 2 m s^{-1} at 1 s. It can be seen in Figure 4 that the concentration profiles of gases found on the anode surface of case B are similar to those of case A as shown in Figure 4.2. When a step change of inlet velocity at 1 s occurs, CO and H_2 generated by the steam reforming reaction are increased immediately. This implies that the steam reforming reaction takes place immediately when the step change occurs. Afterwards, there is a drop of CO concentration before entering the steady state as it is converted into H_2 and CO_2 by the water-gas shift reaction. At the same time, a drop of H_2 concentration is observed indicating that H_2 is consumed by the electrochemical reaction on

the anode side before reaching its steady state at 110 s. It is found that the step change of inlet velocity has an effect on the gas concentration just only during the first few seconds. After that, the concentration of gases are gradually reduced until entering the steady state.

Plots of anode surface temperature against time can be illustrated in Figure 4.5 at different locations (x) along the anode surface. The temperature profiles of case B are similar to those of case A. However, it has been found that the temperature varies from 847 to 1142 K, equal to temperature difference of 295 K which is 60 K lower than that of case A. This is because a step change of velocity from 1 to 2 m s^{-1} at 1 s results in smaller amount of heat produced by the reaction during the start-up. Temperature of anode at x = 0.05 m takes approximately 170 s to reach its steady state.

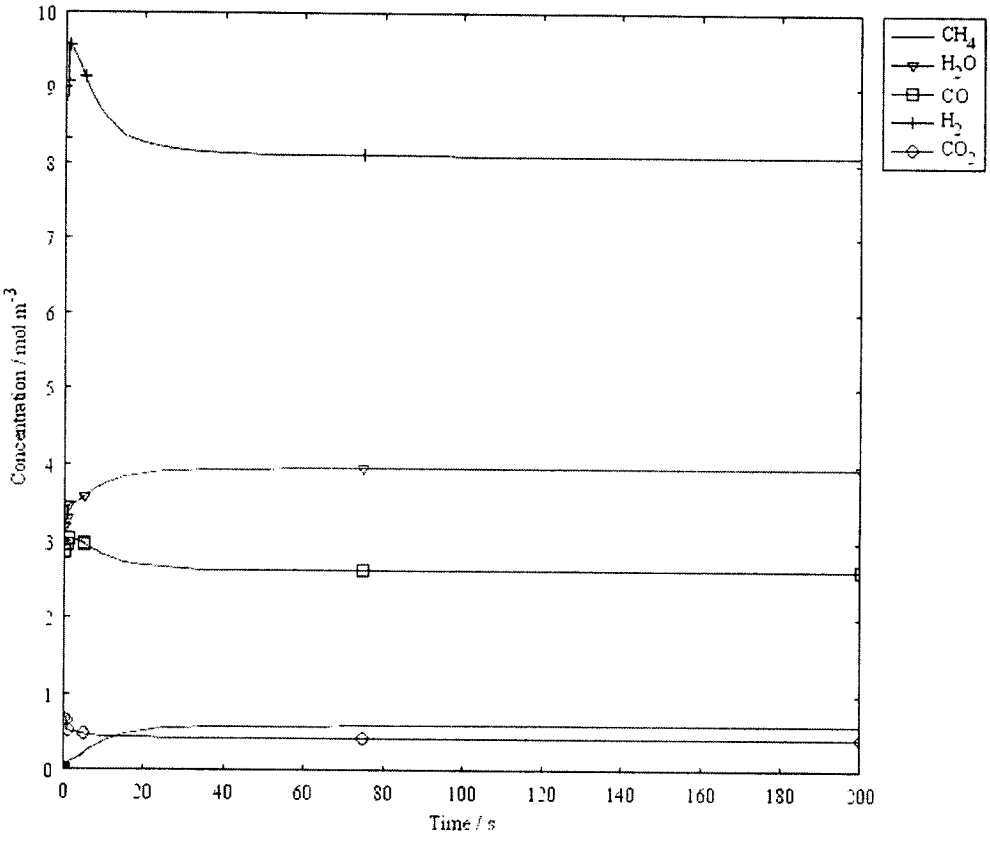

Figure 4.4. Concentration profiles of gases in case B against time at x = 0.01 m.

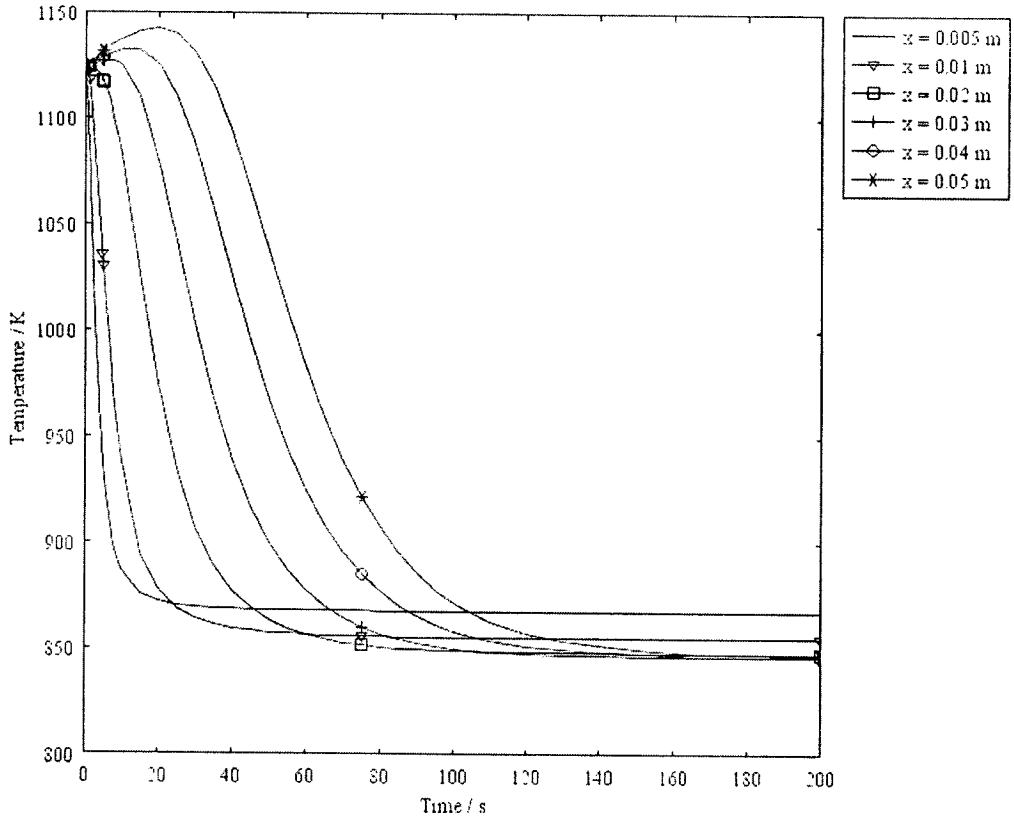

Figure 4.5. Temperature profiles of case B against time

Figures 4.6 and 4.7 of case C illustrate the concentration of gases and the temperature at the anode surface when two step change of inlet velocity is considered. The inlet velocity is jumped from 1 to 1.5 m s^{-1} at 1 s and from 1.5 to 2 m s^{-1} at 5 m s^{-1}.

Gas concentration along the anode surface is plotted against time as depicted in Figure 4.6. It can be seen that the concentration profiles of gases in case C as seen in Figure 4.6 are similar to those of cases A and B as illustrated in Figures 4.2 and 4.4, respectively. When two step change of inlet velocity at 1 and 5 s occur, CO and H_2 generated by the steam reforming reaction are increased immediately. CO is subsequently reduced as it is converted into H_2 and CO_2 by the water-gas shift reaction before reaching the steady state. At the same time, a drop of H_2 concentration is found, indicating that H_2 is consumed by the electrochemical reaction on the anode side before reaching its steady state at 105 s. It is observed that two step change of inlet velocity has an effect on the gas concentration just only at the beginning of operation time. After that, the concentration of gases are gradually reduced towards the steady state.

Plots of anode surface temperature against time of case C can be illustrated in Figure 4.7. At different locations (x) along the anode surface, the temperature profiles of case C with the two step change are similar to those of cases A and B as depicted in Figures 4.3 and 4.5,

respectively. However, it has been found that the temperature ranges from 847 to 1142 K, equal to temperature difference of 295 K which is 60 K lower than that of case A. This is because introducing a step change of velocity from 1 to 1.5 m s^{-1} at 1 s and from 1.5 to 2 m s^{-1} results in smaller amount of heat produced by the reactions during the start-up period. It takes approximately 160 s for the temperature of anode surface at x = 0.05 m to reach its steady state.

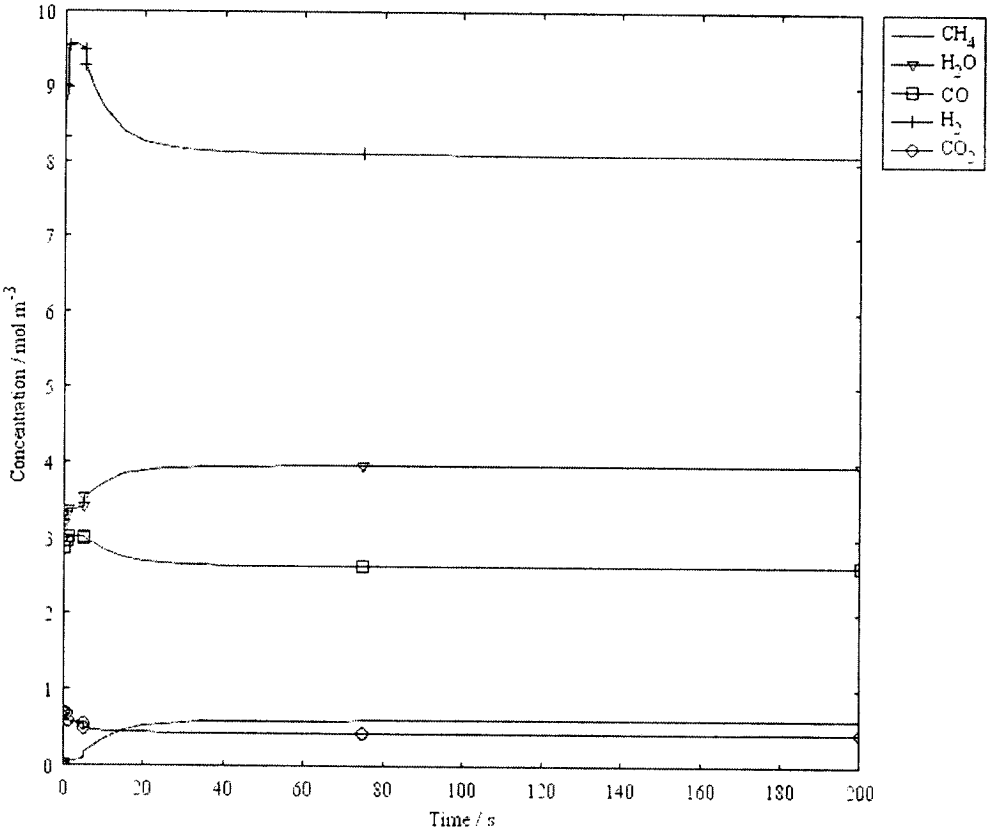

Figure 4.6. Concentration profiles of gases in case C against time at x = 0.01 m.

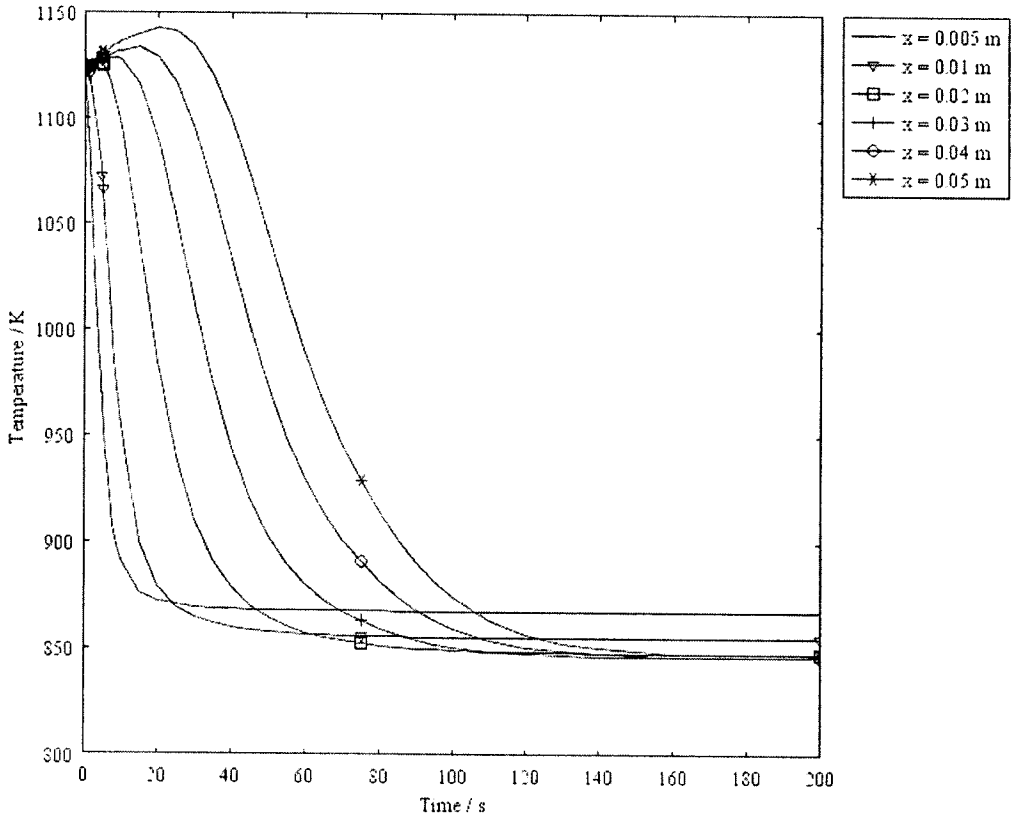

Figure 4.7. Temperature profiles of case C against time

The comparison of H_2 concentration among cases A, B and C are compared in Figure 4.8. It can be seen that neither one nor two step change of inlet velocity does not show a significant change of H_2 concentration after compared with that of case A. This is because steam reforming, water-gas shift and electrochemical reactions are immediately taken place in the flow channel. However, the temperature difference along the anode channel shows a considerable difference among cases A, B and C. Cases B and C perform a good management of temperature difference better than that of case A without a step change. This is because less heat is generated when step change is applied to the fuel flow. It is also found that with step change in velocity, the concentration and temperature profiles of cases B and C move to steady state slightly earlier than those of case A without step change.

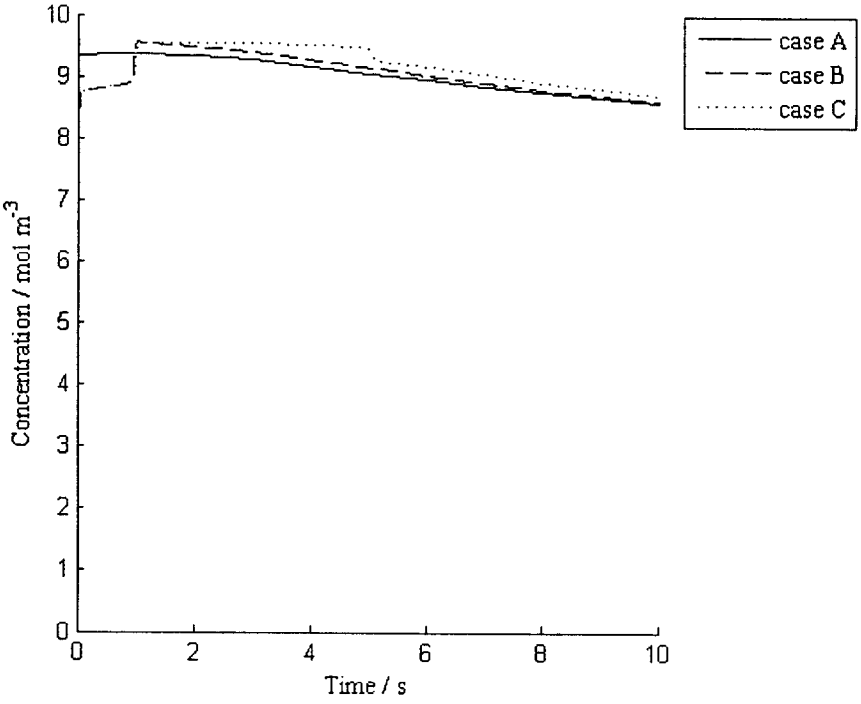

Figure 4.8. H_2 concentration of case A, B and C at x = 0.01 m.

4.3.3. Analysis of transient condition with step change of temperature

In this section, the transient behaviours of the SOFC are investigated through cases D and E due to step changes of fuel inlet temperature at the entrance of the fuel channel. In case D, the inlet temperature is initially maintained at 1023 K. The temperature is then jumped from 1023 to 1123 K at 1 s. Fuel inlet velocity is kept constant at 2 m s^{-1} and initial and operating conditions are considered as shown in Table 4.2. In case D, two step change is applied to the fuel inlet temperature. Initially the temperature is initially maintained at 1023 K. It is then jumped from 1023 to 1073 at 1 s and from 1073 to 1123 K at 5 s. The results of cases D and E are then discussed and compared with those of case A.

The concentration of gases and anode temperature of case D are plotted in Figures 4.9 and 4.10 when a step change of fuel inlet temperature from 1023 to 1123 K is considered. It can be seen that the concentration profiles of gases in Figure 4.9 behave in the same patterns as those of case A as seen in Figure 4.2. However, insignificant difference between cases D and A in gas concentration still can be found during the beginning of the operation. H_2 is generated from the steam reforming and water-gas shift reactions. It is then consumed by the electrochemical reaction so that the concentration is decreased until it reaches the steady state at 95 s which is earlier than that of case A.

Plots of anode surface temperature against time in case D can be illustrated in Figure 4.10 at different locations (x) along the anode surface. The temperature profiles of case D are similar to those of case A, but with smaller temperature difference. The temperature is reduced rapidly near the channel entrance due to the endothermic effect of the steam reforming reaction. It varies from 847 to 1031 K, equal to the temperature difference of 184 K which is much lower than that of case A. This is because applying a step change of temperature from 1023 to 1123 K at 1 s results in smaller amount of heat produced by the reaction during the start-up period. It takes approximately 170 s for the temperature at the anode surface at x = 0.05 m to reach its steady state.

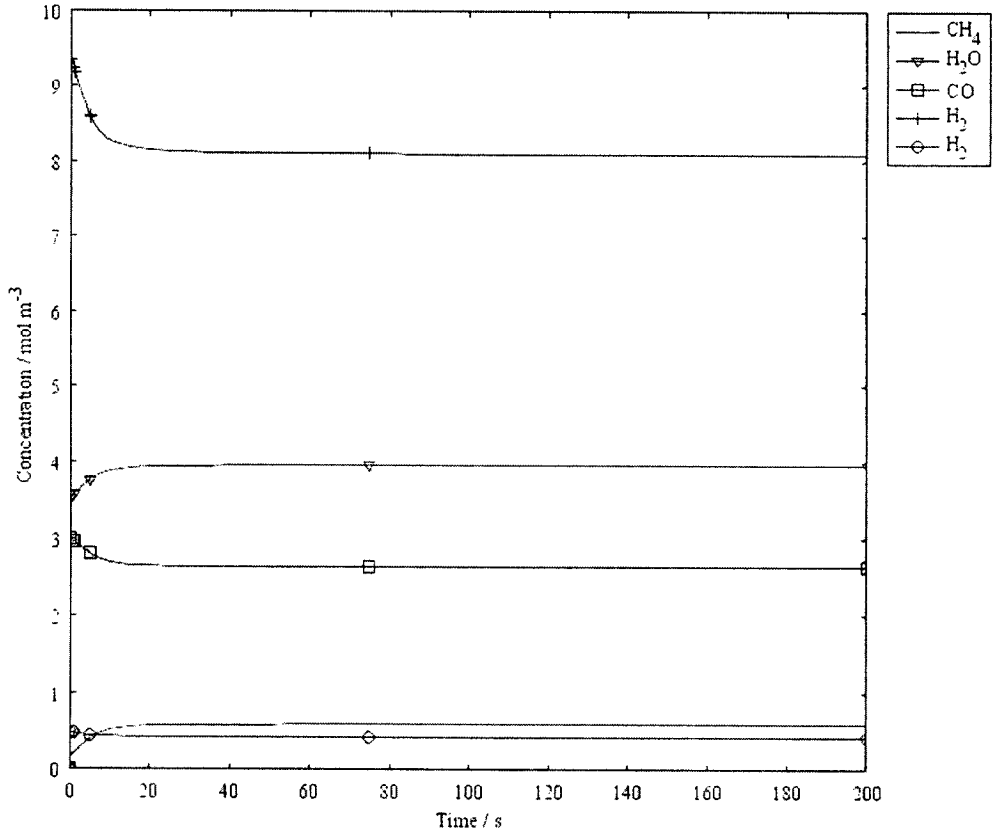

Figure 4.9. Concentration profiles of gases in case D against time at x = 0.01 m.

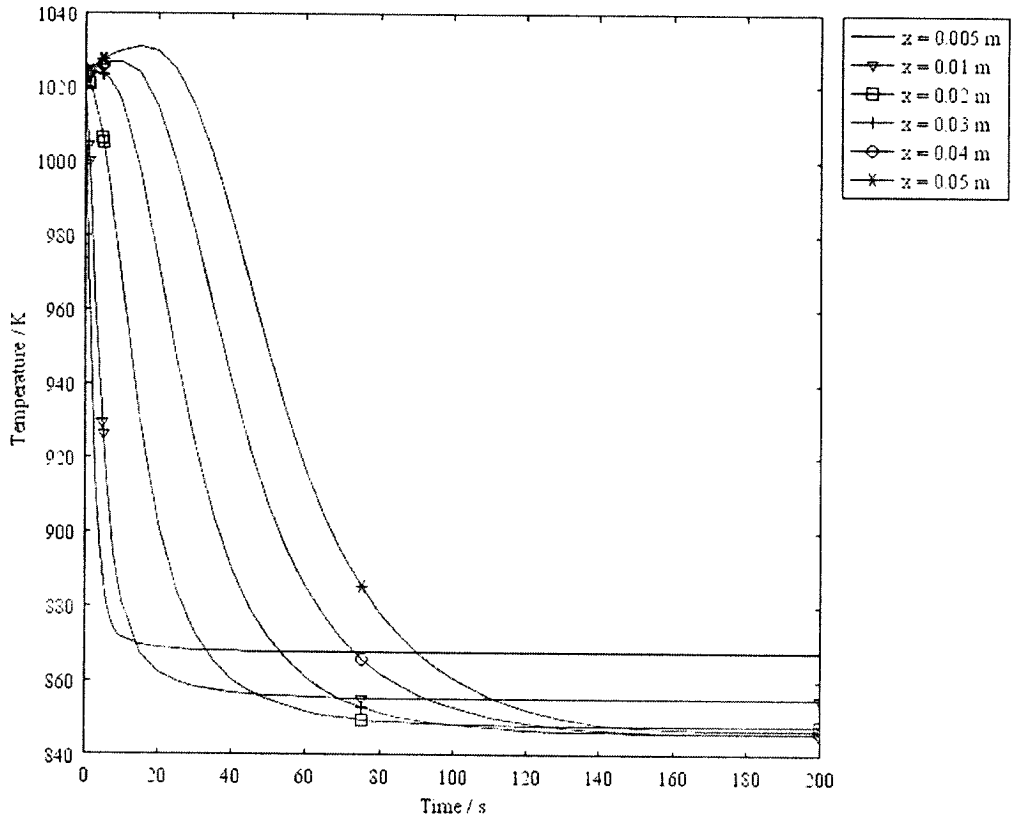

Figure 4.10. Temperature profiles of case D against time

Two step change of fuel inlet temperature is applied to case E and the results are depicted in Figures 4.11 and 4.12. Initially the temperature is set to 1023 K. It is then jumped from 1023 to 1073 at 1 s and from 1073 to 1123 K at 5 s. Similar patterns of concentration to those of case A are found in Figure 11. Beyond the start-up, the two step change does not show a significant effect on the change of gas concentration. H_2 concentration reaches its steady state at 90 s.

The temperature profiles of case E with two step change of inlet temperature as seen in Figure 4.12 are similar to those of cases A and D as illustrated in Figures 4.3 and 4.10, respectively. In the vicinity of the channel entrance, the temperature of anode surface is decreased sharply due to the strongly endothermic effect of the steam reforming reaction. The temperature varies from 847 to 1030 K, equal to the temperature difference of 183 K. This is because a step change of temperature from 1023 to 1073 K and from 1073 K at 1 s to 1123 K at 5 s result in smaller amount of heat produced by the reaction during the start-up period. It takes approximately 160 s for the temperature at the anode surface at x = 0.05 m to reach its steady state.

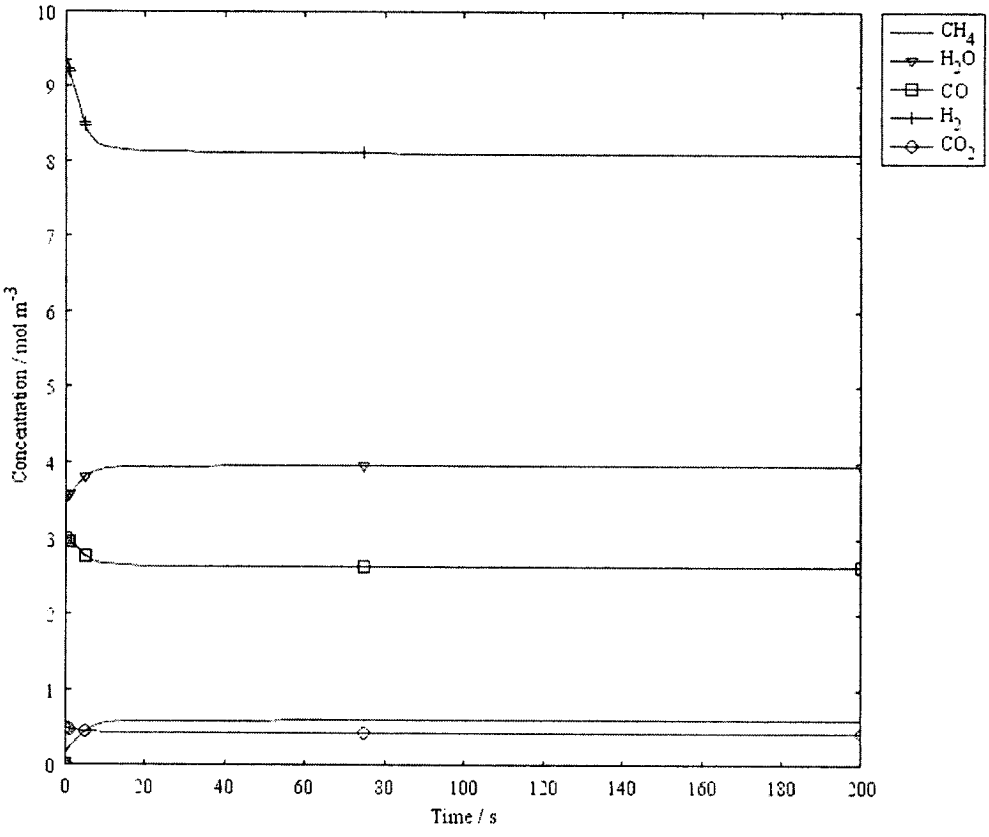

Figure 4.11. Concentration profiles of gases in case E against time at x = 0.01 m.

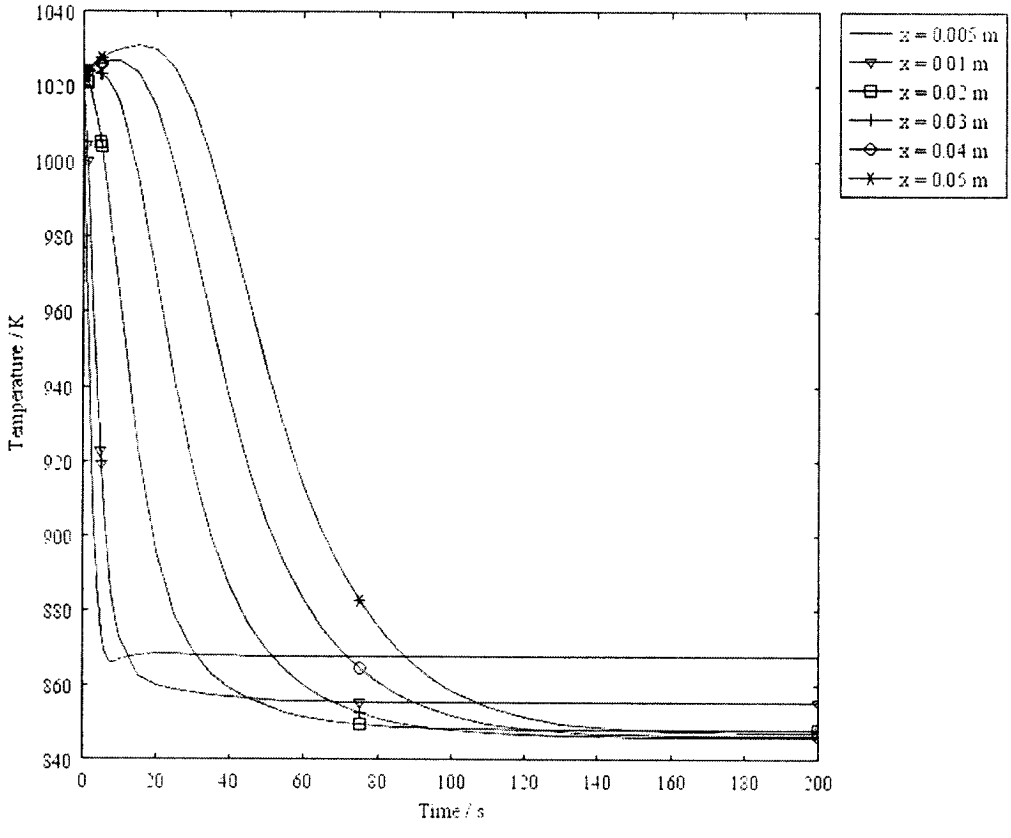

Figure 4.12. Temperature profiles of case E against time

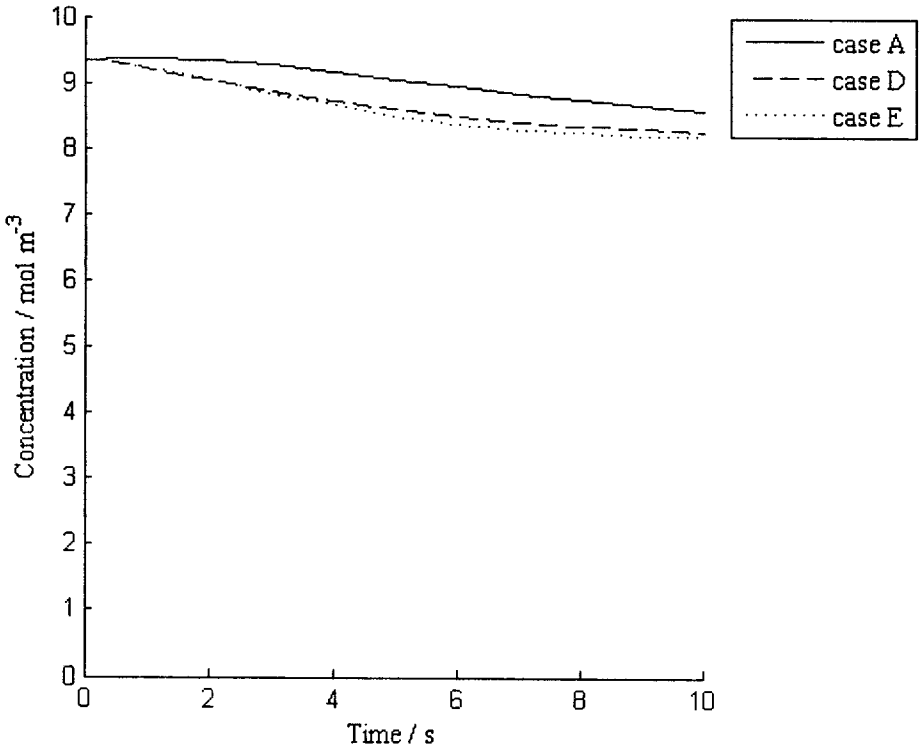

Figure 4.13. H_2 concentration of cases A, D and E at x = 0.01 m.

The comparison of H_2 concentration among cases A, D and E are compared in Figure 4.13. It can be seen that both one and two step change of inlet temperature demonstrate a small difference of H_2 concentration after compared with that of case A. This is because the lower temperature results in the lower rate of reaction, leading to the smaller amount of H_2 produced. However, beyond the start-up period, the flow patterns of gases are almost identical. In the mean time, the temperature difference along the anode channel shows a considerable difference among cases A, D and E. Cases D and E perform a temperature management better than that of case A without a step change. This is because less heat is generated when step change is applied to the fuel flow. It is also found that with step change in temperature, the concentration and temperature profiles of cases D and E move to steady state slightly earlier than those of case A without step change.

5. Conclusions

This work starts with a study of the kinetics of steam reforming, water-gas shift and electrochemical reactions inside the anode flow channel of the SOFC. From the results, it can be found that the kinetics simulated in this work agree well with the phenomena occurred inside the anode channel. The concentration of CH_4 drops dramatically near the inlet as CH_4 is completely converted, meaning that, at the inlet of a cell, the reforming rate dominates such that the inlet region cools below the feed temperature. The consumption of H_2O in the steam reforming and water-gas shift reactions leads to a decrease in H_2O concentration near the inlet. At the same time, CO, H_2 and CO_2 concentration gradually increases. As the reaction proceeds, CO_2 is increased with a gradual decrease of H_2 consumed by the electrochemical reaction and CO used in the water-gas shift reaction. H_2O produced by oxidation reaction is also increased because the electrochemical reaction eventually dominates over the steam reforming and water-gas shift reactions.

The temperature is decreased dramatically near the inlet of the flow channel due to the highly endothermic steam reforming reaction. The steep temperature gradients that result from the localised cooling within the cell can lead to significant thermal stresses in the solid structure and potentially to a system failure from crack formation in the cell. Therefore, cautious operation should be concerned operating the SOFC.

In order to prevent the carbon deposition, increasing the inlet steam mass fraction or a steam to carbon ratio has come to a consideration. The steam to carbon ratios of 2:1, 3:1, 4:1 and 5:1 are examined in this work. It can be concluded that the steam to carbon ratio of 2:1 shows the preferable results among other ratios. This is due to the highest amount of CH_4 found at the inlet; therefore, the higher rate of reaction can be predicted.

The effect of anode porosity on the kinetics of steam reforming, water-gas shift and electrochemical reactions corresponding to gas species, heat and current density distributions inside the SOFC are also studied. From the results, it can be found that porosity has massive influences on the gas species, the temperature and the current density variation. The increase of anode porosity enhances the rate of reforming reaction, rate of shift reaction, amount of CH_4 diffused through the anode and amount of H_2 produced. However, the increase of anode porosity decreases the amount H_2 consumption and CO consumption along the anode depth. It also reduces the temperature and the current density along the anode surface. An increase in anode porosity enhances the effective diffusivity and the permeability, but decreases the tortuosity, the reactive surface area, the effective electronic and ionic conductivity, and therefore, the current density. It can be concluded that maintaining the low porosity should give the best performance of the cell

when considering the current density produced. However, this has to bear in mind that the results of this work is based on the fact that the radii of both electron conducting particles and ion conducting particles are fixed at 0.1 μm, implying that the increase in porosity causes the increase of void fraction, therefore, the reactive surface area is decreased.

The transient behaviours of the solid oxide fuel cell have been studied in this work. The fuel flow consisting of CH_4 and H_2O is fed into the anode flow channel where the direct steam reforming and water-gas shift reactions occur inside the anode flow channel. The transient behaviours have been studied in 3 major cases, one without disturbance, one with step changes of fuel flow inlet velocity and one with step changes of the fuel flow inlet temperature. For the latter two cases, both one and two step change are investigated and the results are compared with the case without any disturbance.

When both one and two step changes of inlet velocity are considered, it can be found that, during the start-up period, the jumps of gas concentration are occurred instantaneously with jumps of inlet velocity. Apart from the start-up period, their concentration profiles are almost identical to the case without any disturbance. This is because steam reforming and water-gas shift reactions are immediately taken place as soon as the fuel flow enters the flow channel. The temperature difference of the cases with one and two step changes of inlet velocity are much smaller than the one without any disturbance because less heat is produced during the start-up period. The only difference between the one step and two step changes of inlet velocity is that the gas concentration profiles and anode temperature profiles of the two step change of inlet velocity reaches the steady state slightly earlier than that of the one step change of velocity. This is because gas and heat of the case with two step change are smaller than those of the case with one step change during the start-up period.

When effects of one and two step changes of inlet temperature are applied, less gas is obviously produced after compared with that of the case without any disturbance. However, this only happens during the start-up period. Beyond that period, gas concentration profiles of the cases with step changes of inlet temperature are almost identical to those of the case without any disturbance because the steam reforming and water-gas shift reactions are instantaneously taken place near the fuel channel entrance. The temperature differences of the cases with step changes of inlet temperature are much smaller than that of the case without any disturbance. This is because less heat is produced during the start-up period. This reason also supports how the gas concentration profiles and temperature profiles of the two step change can reach the steady state slightly earlier than those of the one step change.

It can be concluded that insignificant results are found in the gas concentration profiles when step changes of the inlet parameters are applied to the flow channel because the steam reforming and water-gas shift reactions happen rapidly. However, during the start-up period, step changes of operating parameters have a considerable effect on the temperature profiles in the flow channel as less heat is produced for a short period of time. Therefore, this technique can be considered as a tool to lower the temperature difference inside the cell.